Anesthetics fragment hippocampal network activity, alter spine dynamics and affect memory consolidation

Wei Yang[1,6], Mattia Chini[2,6], Jastyn A. Pöpplau[2], Andrey Formozov[1], Alexander Dieter[1], Patrick Piechocinski[1], Cynthia Rais[1], Fabio Morellini[3], Olaf Sporns[4,5], Ileana L. Hanganu-Opatz[2] and J. Simon Wiegert[1*]

[1]Research Group Synaptic Wiring and Information Processing, Center for Molecular Neurobiology Hamburg, University Medical Center Hamburg-Eppendorf, 20251 Hamburg, Germany

[2]Developmental Neurophysiology, Center for Molecular Neurobiology Hamburg, University Medical Center Hamburg-Eppendorf, 20251 Hamburg, Germany

[3]Research Group Behavioral Biology, Center for Molecular Neurobiology Hamburg, University Medical Center Hamburg-Eppendorf, 20251 Hamburg, Germany

[4]Department of Psychological and Brain Sciences, Indiana University, Bloomington, Indiana, USA

[5]Indiana University Network Science Institute, Indiana University, Bloomington, Indiana, USA

[6]These authors contributed equally

*Correspondence: simon.wiegert@zmnh.uni-hamburg.de, @SimWieg, ORCID: 0000-0003-0893-9349

ABSTRACT

General anesthesia is characterized by reversible loss of consciousness accompanied by transient amnesia. Yet, long-term memory impairment is an undesirable side-effect. How different types of general anesthetics (GAs) affect the hippocampus, a brain region central to memory formation and consolidation, is poorly understood. Using extracellular recordings, chronic 2-photon imaging and behavioral analysis, we monitor the effects of isoflurane (Iso), medetomidine/midazolam/fentanyl (MMF), and ketamine/xylazine (Keta/Xyl) on network activity and structural spine dynamics in the hippocampal CA1 area of adult mice. GAs robustly reduced spiking activity, decorrelated cellular ensembles, albeit with distinct activity signatures, and altered spine dynamics. CA1 network activity under all three anesthetics was different to natural sleep. Iso anesthesia most closely resembled unperturbed activity during wakefulness and sleep, and network alterations recovered more readily than with Keta/Xyl and MMF. Correspondingly, memory consolidation was impaired after exposure to Keta/Xyl and MMF, but not Iso. Thus, different anesthetics distinctly alter hippocampal network dynamics, synaptic connectivity, and memory consolidation, with implications for GA strategy appraisal in animal research and clinical settings.

KEYWORDS

General anesthesia, isoflurane, ketamine, fentanyl, sleep, hippocampus, population dynamics, network activity, spine turnover, episodic memory

INTRODUCTION

General anesthesia is a drug-induced, reversible behavioral condition encompassing unconsciousness, amnesia, sedation, immobility, and analgesia [1, 2]. Together, these aspects represent a state where surgery can be tolerated without the requirement for further drugs [2]. The behavioral effects of GAs are dose-dependent. At clinical (i.e. highest) dosage, they should induce unconsciousness, even though experimental evidence of this phenomenon is challenging to collect (in the absence of a verifiable consciousness theory). At lower doses, some GAs cause unresponsiveness and loss of working memory, phenomena that have both been hypothesized to potentially confound the apparent loss of consciousness [3, 4]. At much lower doses still, GAs cause profound retrograde amnesia. When general anesthesia fails to induce such behavioral effects, intraoperative awareness ensues, a condition that is associated with long-term adverse health consequences [5]. While loss of memory is required during anesthesia administration, so that no memories of the surgical procedure are formed [1, 6], long-term impairment of retrograde or anterograde memories is not desired. Although general anesthesia is generally considered a safe procedure, growing literature points to the possibility of long-term negative effects on the central nervous system [7]. This is particularly true for specific categories of patients, such as the elderly, infants and children [7]. Among the observed side effects, the most common are post-operative cognitive dysfunction syndromes, including post-operative delirium and post-operative cognitive decline. Post-operative cognitive disturbances are positively correlated with the duration of anesthesia and a single exposure to GAs can cause retrograde and anterograde memory deficits that persist for days to weeks in rodent models [8]. These aspects point to a generalized action of GAs on the memory system.

Given that amnesia is a fundamental part of general anesthesia and that the hippocampus controls memory formation and consolidation, it is important to understand how anesthetics affect hippocampal function and how this compares to sleep – a naturally occurring state of unconsciousness. Together with the subiculum, the CA1 area constitutes the main hippocampal output region. CA1 pyramidal cells receive excitatory synaptic input mainly from CA3 (in strata oriens & radiatum) and layer 3 of entorhinal cortex (in stratum lacunosum moleculare), relaying information about the internal state of the animal and sensory inputs from the external environment, respectively [9]. Inputs along these pathways are processed in an integrative manner in CA1 [10]. Thus, CA1 pyramidal cells have been suggested to be a site of sensory integration, with synaptic spines as a possible location of memory storage [11-14]. Moreover, dynamic modulation of spine stability has been linked to synaptic plasticity [15-18]. Synaptic plasticity, in turn, underlies learning and memory formation [19], suggesting that spine turnover in the hippocampus directly reflects these processes [20, 21]. Considering the low concentrations of anesthetics required to induce amnesia, these compounds are thought of being particularly effective on the hippocampus. One possible explanation of this sensitivity is the fact that a class of γ-aminobutyric acid receptors (GABARs), which is strongly modulated by some anesthetics, is predominantly expressed in the hippocampus [22, 23]. Other anesthetics, such as ketamine, inhibit N-methyl-D-aspartate receptors (NMDARs) in a use-dependent manner and therefore may be particularly effective in inhibiting synaptic plasticity, required for the formation of episodic-like memories [24]. However, a systematic investigation of the effects of anesthetics on the hippocampus, bridging synaptic, network and behavioral levels, is still lacking.

Here, using extracellular LFP and spiking recordings and chronic 2-photon calcium and spine imaging in vivo in combination with behavioral analysis, we systematically assessed how CA1

88   network dynamics, synaptic structure and memory performance are affected by three
89   commonly used combinations of GAs: isoflurane (Iso), midazolam/medetomidine/fentanyl
90   (MMF), and ketamine in combination with xylazine (Keta/Xyl). We further measured CA1
91   network dynamics during wakefulness and natural sleep. Unlike sleep, all three GAs strongly
92   reduced overall neuronal spiking compared to wakefulness. Moreover, opposite to what has
93   been found in the neocortex [25-27], they decorrelated network activity, leading to a
94   fragmented network state. However, the induced patterns of activity were highly distinct
95   between the three different anesthetic conditions and recovered to the pre-anesthetic status
96   with disparate rates. Testing the effect of repeated anesthesia on spine dynamics revealed
97   that Keta/Xyl, the condition which most strongly affected calcium activity, significantly reduced
98   spine turnover, leading to an overall (over)stabilization of hippocampal synapses. In contrast,
99   Iso and MMF mildly increased spine turnover. Finally, we show that the two anesthetic
100 conditions which induce the strongest reduction and fragmentation of CA1 network activity,
101 Keta/Xyl and MMF, negatively influenced hippocampus-dependent memory consolidation. On
102 the other hand, Iso, which most closely resembled unperturbed sleep and wakefulness, did not
103 impair memory consolidation, even when maintained over time periods matching the longer
104 recovery phase of Keta/Xyl or MMF. Thus, different anesthetics, despite inducing a similar
105 physiological state, strongly differ in their effects on synaptic stability, hippocampal network
106 activity, and memory consolidation.

107

108 **RESULTS**

109 **Iso, Keta/Xyl and MMF induce distinct patterns of network activity**

110 Iso, Keta/Xyl and MMF have distinct molecular targets and modes of action in the brain. We
111 therefore hypothesized that electrical activity in the hippocampus might be uniquely altered by
112 the three anesthesia strategies. To test this hypothesis, we investigated local field potentials
113 (LFPs) and firing of individual neurons (single-unit activity, SUA) extracellularly recorded in the
114 CA1 area of the dorsal hippocampus (dCA1) during wakefulness, followed by 45 min of
115 anesthesia and 45 min of recovery (Fig. 1A, S1A). We found that the anesthetics differently
116 affected population activity, inducing characteristic modulation of various frequency bands
117 (Fig. 1B). During wakefulness, LFP power in CA1 was highest in the theta (4-12 Hz) and low-
118 gamma (40-60 Hz) frequency bands (Fig. S1B). Exposure to 2-2.5% Iso led to a strong
119 reduction of LFP power > 4 Hz within the first 2 minutes, which was accompanied by complete
120 loss of mobility of the animal (Fig. 1C, S1B,C). Similarly, MMF injection promptly decreased
121 LFP power in the same frequency bands. In contrast, Keta/Xyl increased power across all
122 frequencies during the first 10 min after injection, the most prominent effect being observed for
123 activity at 5-30 Hz. This is consistent with previous reports, finding enhanced theta and low-
124 gamma power in CA1 of rats under ketamine anesthesia [28]. The initial LFP power increase
125 was followed by a gradual, significant decrease of 30-100 Hz activity (Fig. 1C, S1B,C).

126 It is widely accepted that, in the neocortex, GAs favor slow oscillations at the expense of faster
127 ones [29]. To determine whether this is also the case in the hippocampus, we next asked how
128 the investigated anesthetics affect slow network oscillations. Consistent with previous reports
129 [30-32], Keta/Xyl strongly enhanced LFP power at 0.5-4 Hz throughout the entire recording
130 period (Fig. 1C,D, S1C), but suppressed frequencies lower than 0.5 Hz. In contrast, Iso
131 strongly augmented LFP power below 0.5 Hz, peaking at 0.1-0.2 Hz (Fig. 1C,D, S1C), whereas
132 MMF induced no significant increase in the low-frequency regime. However, similar to
133 Keta/Xyl, a significant reduction was present below 0.5 Hz, which persisted throughout the

3

134 entire recording period (Fig. 1C,D). Analysis of the power-law decay exponent (1/f slope) of
135 the LFP power spectrum facilitates detection of non-canonical changes in LFP power, including
136 aperiodic (non-oscillatory) components [33]. The 1/f slope has been hypothesized to track
137 excitation/inhibition (E/I) balance [34, 35], and is reduced in the cortex under anesthesia [36,
138 37], indicating a shift towards inhibition. Considering the robust effects on LFP power that we
139 reported, we reasoned that the 1/f slope might also be altered. Indeed, all anesthetics
140 significantly decreased the 1/f slope, albeit with a different temporal profile. While the effect of
141 Iso occurred within a few minutes, MMF and Keta/Xyl operated on a longer timescale (Fig. 1E).
142 Moreover, periods of activity were consistently and strongly reduced immediately under Iso
143 and MMF, but delayed by 30 min under Keta/Xyl (Fig. 1F). These results indicate that all
144 anesthetics shift the LFP to lower frequencies and tilt the E/I balance towards inhibition, albeit
145 with different temporal profiles.

146 In contrast to Keta/Xyl-anesthesia, Iso- and MMF-anesthesia can be efficiently antagonized.
147 Removing the face mask is sufficient to antagonize Iso-anesthesia, while antagonization of
148 MMF-anesthesia requires injection of a wake-up cocktail (Flumazenil, Atipamezole and
149 Buprenorphine, FAB) [38, 39]. 20-30 min after Iso withdrawal, animals regained motility and
150 periods of silence in the LFP receded (Fig. 1C,F). However, in contrast to post-Iso, LFP power
151 did not fully recover after FAB, remaining significantly reduced at frequencies below 0.5 and
152 above 30 Hz for the entire 45 min-post anesthesia recording period (Fig. 1C,D). In contrast,
153 elevated LFP power in the 0.5-4 Hz band and reduction in active periods remained significant
154 throughout the entire recording in the presence of Keta/Xyl. In line with these results, the 1/f
155 slope promptly reverted to values similar to baseline after Iso discontinuation. In contrast, the
156 recovery was only transitory and partial after MMF antagonization, and virtually absent for
157 Keta/Xyl (Fig. 1E), indicating that the E/I balance recovered only after Iso within 45 min.

158 Cross-frequency coupling between theta and gamma oscillations has been suggested to
159 underlie information transfer in the hippocampus [40]. Given the strong decrease of theta
160 power in the presence of Iso and MMF, we reasoned the phase modulation of the gamma
161 rhythm could also be altered. To test this, we used phase-amplitude coupling (PAC) to
162 measure whether the phase of slow LFP oscillations modulates the amplitude of the signal at
163 a higher frequency. In line with previous results [41, 42] a significant coupling between theta
164 and gamma frequency bands, as well as between frequencies in the 1-2 Hz range and gamma
165 was present in the awake state (Fig. 1G). Moreover, anesthesia strongly altered PAC. In
166 accordance with the LFP power analysis, the coupling reached a maximum strength between
167 the dominant slow-frequency oscillations induced by the various anesthetics (<0.5 Hz for Iso,
168 ~1 Hz for MMF and 0.5-4 Hz for Keta/Xyl) and gamma (Fig. 1G). For all anesthetics, the range
169 of phase-modulated amplitudes was wide, suggesting that the modulating phase corresponds
170 to the identified slow-wave activity.

171 Taken together, these data show that all three GAs differently and persistently modulated the
172 network oscillations in dCA1, a full recovery of activity being detected within 45 min only for
173 Iso.

4

174
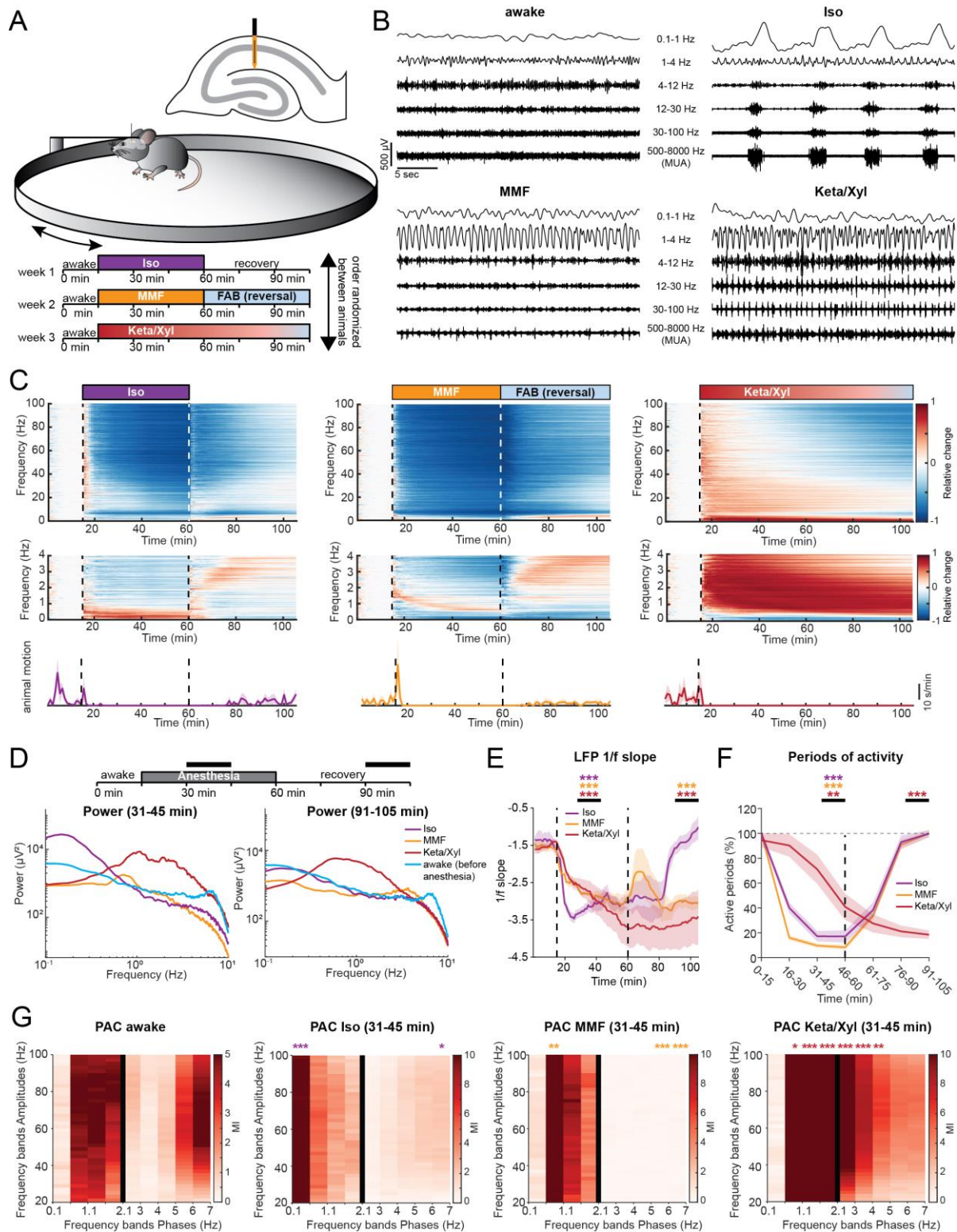
Figure 1: LFP recordings in dorsal CA1 during wakefulness and anesthesia reveal distinct and complex alterations by Iso, Keta/Xyl and MMF. (A) *Experimental setup. Extracellular electrical recordings in dorsal CA1 were performed in four head-fixed mice for 105 min, continuously. Each animal was recorded under all anesthesia as indicated in the scheme. Order of anesthetics was pseud-randomized.* **(B)** *Characteristic local field potential (LFP) recordings during wakefulness and under three different anesthetics.* **(C)** *Color-coded modulation index (MI) plots (upper and middle panels) for LFP power and motion profiles (lower panels) for the three different anesthetic conditions. Upper panels display LFP power for 0-100 Hz frequency range, lower panels for 0-4 Hz.* **(D)** *Line plot displaying LFP power spectra for the two time periods indicated by horizontal black bars. For comparison, the 15-min*

184 *spectrum of the awake period before anesthesia induction is plotted in both graphs. Statistical*
185 *differences are indicated in Fig. S1C (E) Line plot displaying the power-law decay exponent (1/f) of the*
186 *LFP power spectrum for the 30-50 Hz range. Lines display mean ± SEM. (F) Line plot displaying the*
187 *fraction of active periods compared to the pre-anesthetic wakeful state, in 15 min bins throughout the*
188 *entire recording duration. Lines display mean ± SEM. (G) Heat map displaying Phase-amplitude-*
189 *coupling (PAC) for pre-anesthetic wakeful state (left) and for the indicated time periods during*
190 *anesthesia. Different bin sizes (0.5 Hz and 1 Hz, separated by vertical black line) are used to resolve*
191 *low- and high-frequency PAC. Vertical dashed lines in (C) and (E) indicate time points of anesthesia*
192 *induction (Iso, MMF, Keta/Xyl) and reversal (Iso & MMF only). Vertical dashed line in (F) indicates time*
193 *point of anesthesia reversal (Iso & MMF only). Asterisks in (E) and (F) indicate significance of time*
194 *periods indicated by black horizontal line compared to 15-min period before anesthesia. Anesthetic*
195 *conditions are color-coded. Asterisks in (G) indicate significant differences compared to the*
196 *corresponding frequency band during wakefulness. * p < 0.05, ** p < 0.01, *** p < 0.001, n = 4 mice. For*
197 *full report of statistics, see statistics table.*

198

## Delayed recovery of neuronal spiking patterns after anesthesia

200 While the LFP provides information about general network states in the hippocampus, it is
201 influenced by long-range activity and highly active regions in the vicinity of CA1 [43]. To assess
202 the effects of GAs on CA1 neurons, we analyzed the spiking of individual units (56-72 units
203 per animal, n=4 mice) before, during and after each of the anesthetic conditions. All anesthetics
204 significantly and rapidly (<1 min) decreased spiking activity in CA1 neurons (Fig. 2A,B, S2),
205 with MMF leading to the most potent suppression, followed by Iso and Keta/Xyl. These
206 alterations were generally present in all layers of CA1 (Fig. S2C). Although the bulk spike rate
207 was strongly reduced, the number of active neurons (see Methods) was only mildly affected
208 (Fig. 2C), reaching a significant reduction only with MMF. This observation suggests that
209 anesthesia broadly reduces neuronal activity, and does not modulate only a discrete
210 subpopulation of neurons. Both firing rate and the number of active neurons recovered within
211 45 min after reversal for MMF and Iso (Fig. 2A-C, S2). As previously reported for NREM sleep
212 [44], we found a negative correlation between the anesthesia-induced reduction of firing rate
213 and the firing rate in wakefulness (Fig S2B).

214 To investigate whether the rhythmicity of single neuron firing was affected similarly to the LFP,
215 we analyzed the spectral properties of 1 ms-binned SUA firing (i.e., power of SUA spike trains,
216 for details, see Methods). In the presence of Iso, SUA power was consistently increased in the
217 range between 0 and 0.5 Hz (Fig. 2A,D, S2), in line with the strong modulation of LFP at 0.1-
218 0.2 Hz. Of note, this effect did not vanish after Iso removal, suggesting that Iso has a long-
219 lasting impact on firing rhythmicity. In contrast, and in line with its effects on the LFP, MMF
220 generally reduced, albeit less strongly, SUA power, including the low frequencies. A significant
221 reduction of SUA power was still present 45 min after antagonization in the 0-0.5 Hz band.
222 Keta/Xyl, on the other hand, only showed a tendency towards reduced SUA power in the
223 frequency band below 0.5 Hz, but increased SUA power significantly in the range between 0.5
224 and 4 Hz, consistent with its effect on the LFP (Fig. 2D). This modulation was present
225 throughout the entire recording. At higher frequencies, Iso led to a peak in the theta frequency
226 range, similar to wakefulness (Fig. 2E), yet it reduced the SUA power in the beta/gamma range.
227 Keta/Xyl and MMF caused an overall reduction in SUA power at frequencies >5 Hz (Fig. 2E).
228 Thus, GAs differentially impair spiking rhythmicity. These changes appeared to follow similar
229 dynamics than those in the LFP.

230 To confirm the synchrony between spikes and low-frequency oscillations, we calculated their
231 pairwise phase consistency (PPC) [45]. When compared to pre-anesthesia, PPC values for
232 the 0.1-0.5 Hz frequency band were augmented by Iso. Keta/Xyl increased coupling of spikes
233 to the LFP between 0.5 and 1 Hz, whereas MMF showed a weak, but significant increase of
234 coupling at frequencies below 1 Hz (Fig. 2F).

235 Similar to the LFP, the SUA firing rate nearly fully recovered during the 45 min post-Iso (Fig.
236 2A,B, S2), with even a slight, but significant increase at the end of the recording period. In
237 contrast, after FAB-induced MMF reversal, CA1 spiking activity remained slightly reduced,
238 reflecting the lack of LFP recovery. For Keta/Xyl, SUA remained suppressed during the entire
239 recording period (Fig. 2B). Strikingly, SUA power did not fully recover for any of the tested
240 anesthetics (Fig. 2E).

241 Taken together, we show that all investigated GAs caused a persistent and robust reduction
242 of CA1 firing. Moreover, spiking during anesthesia was phase-locked to the GA-induced slow
243 network oscillations.
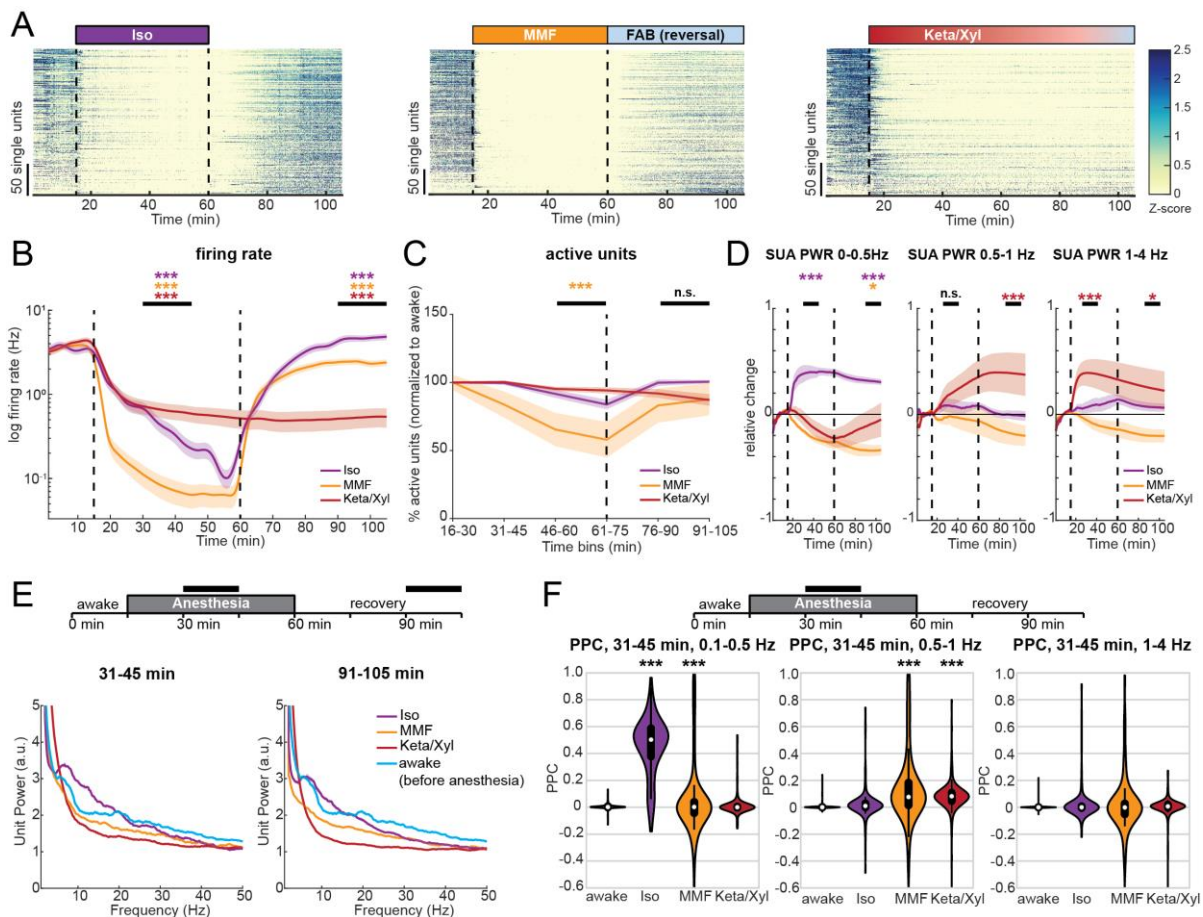
244

245 **Figure 2: Single unit activity in dorsal CA1 is strongly reduced during anesthesia, and remains
246 significantly altered long after its termination. (A)** *Raster plots of z-scored single-unit activity (SUA)
247 for the three different anesthetic strategies in four mice. Units are sorted according to initial activity
248 during wakefulness. **(B)** Line plot of SUA firing rate before, during and after anesthesia induction. **(C)**
249 Line plot displaying the fraction of active units compared to the pre-anesthetic wakeful state, for all three
250 anesthetics in 15 min bins throughout the entire recording duration. **(D)** Relative change of population
251 firing rate power in the 0-0.5, 0.5-1 and 1-4 Hz frequency band. SUA PWR = power of SUA spike trains.
252 **(E)** Line plot displaying the normalized power spectra of population firing rate for the two time periods
253 indicated by horizontal black bars. For comparison, the 15-min spectrum for pre-anesthetic wakeful state*

7

254   *is plotted in both graphs. (F) Pairwise phase consistency (PPC) at low frequencies in the same frequency*
255   *bands as (D), for the indicated time points during anesthesia. White dots indicate median, vertical thick*
256   *and thin lines indicate 1st-3rd quartile and interquartile range, respectively. Colored lines in (B) - (D)*
257   *display mean ± SEM. Vertical dashed lines in panels (A), (B) and (D) indicate time points of anesthesia*
258   *induction (Iso, MMF, Keta/Xyl) and reversal (Iso & MMF only). The vertical dashed line in (C) indicates*
259   *the time point of anesthesia reversal (Iso & MMF only). Asterisks in (B) - (D) indicate significance of*
260   *periods indicated by black horizontal line compared to period before anesthesia. Anesthetic conditions*
261   *are color-coded. Asterisks in (F) indicate significant differences to wakefulness. * p < 0.05, ** p < 0.01,*
262   **** p < 0.001, n = 4 mice. For full report of statistics, see statistics table.*

263

Iso, Keta/Xyl and MMF reduce number, amplitude, and duration of calcium transients

264

265   To monitor the population dynamics of CA1 neurons in the presence of different anesthetics,
266   we imaged the same field of view (FOV) using the genetically encoded indicator GCaMP6f [46]
267   and systematically compared the activity of identified neurons during quiet wakefulness and in
268   the presence of different anesthetics (Fig. 3A).

269   First, we considered all active neurons in each condition and analyzed the average rate (i.e.,
270   the number of transients), amplitude, and duration (i.e., the decay constant) of calcium
271   transients across all imaging sessions in 7 mice. In line with the results of SUA analysis (see
272   Fig. 2C), a large number of CA1 pyramidal neurons were active in the presence of all three
273   GAs. Using extraction parameters that restricted the number of ROIs but maximized signal
274   quality (see Methods), we obtained a median of 311 (min-max of 16-817) active neurons per
275   FOV, for a total of 189 five-minutes recordings. All GAs significantly altered calcium dynamics
276   in CA1 neurons, reducing the activity (Fig. 3C,D), as previously shown for neuronal spiking
277   (Fig. 2B). Also, in line with the effect on SUA (Fig. S2B), the magnitude of the anesthesia-
278   induced reduction of calcium transients was negatively correlated with the wakefulness
279   calcium transients rate (Fig. S6D). However, each condition could be characterized by a
280   specific signature in their calcium dynamics. Iso yielded only a mild decrease of rate and
281   amplitude, but a strong reduction of duration of calcium transients (Fig. 3D). Consistent with
282   effects on LFP and SUA, calcium transients showed a spectral peak between 0.1 and 0.2 Hz
283   (Fig. S4). In contrast to Iso, MMF did not significantly affect the duration of transients but
284   reduced their rate and amplitude when compared to wakefulness. Keta/Xyl-anesthesia had the
285   strongest effect on calcium transients, leading to a reduction of all three parameters compared
286   to wakefulness (Fig. 3D). Unlike for electrophysiological recordings, no spectral peak was
287   present in calcium transients, most likely due to the strong suppression of calcium activity by
288   Keta/Xyl. Considering all parameters, the four groups tended to segregate into clusters, one
289   consisting mostly of recordings under Keta/Xyl, and another one consisting of awake and Iso
290   recordings. Most recordings under MMF clustered between these two groups (Fig. 3E).
291   Importantly, these findings were robust to changes in the signal extraction pipeline. Varying
292   the threshold for calcium transient detection across a wide range of values did not affect the
293   reported effects on rate and height of transients (Fig. S3B). Further, conducting the same
294   analysis on neuronal activity metrics that are independent of calcium transients detection
295   (integral and standard deviation) or on dF/F calcium signals also yielded analogous results
296   (Fig. S3C-E).

297
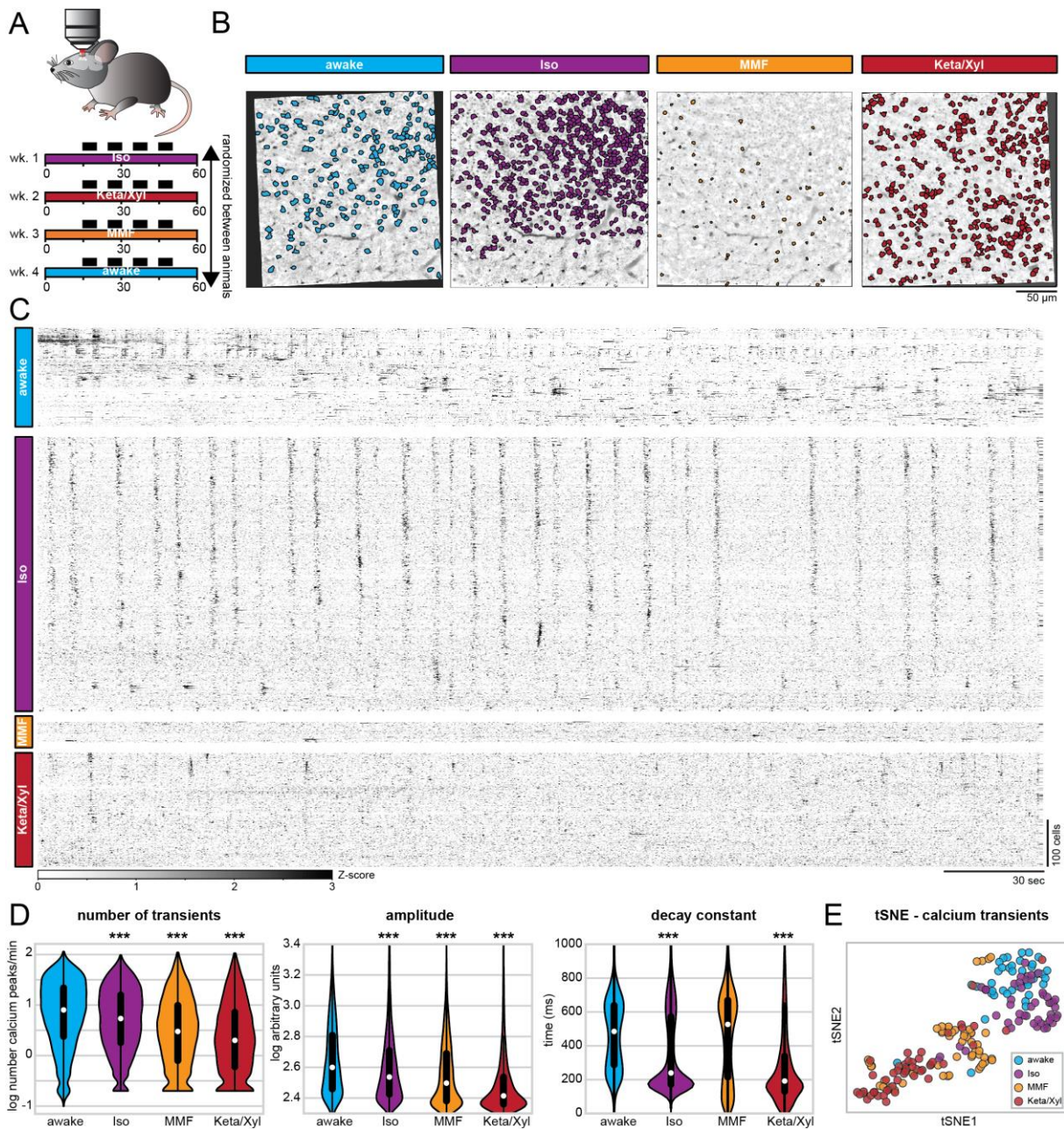
Figure 3: Repeated calcium imaging in dorsal CA1 reveals distinct activity profiles for Iso, MMF and Keta/Xyl. (A) *Experimental strategy for chronic calcium imaging of cellular activity in dorsal CA1. For each condition, seven mice were imaged four times for five minutes, as indicated by black fields in the scheme. The order of imaging conditions was pseudo-randomized.* **(B)** *Time-averaged, two-photon images of the same FOV in CA1 aligned to the Iso condition. ROIs of automatically extracted, active neurons are overlaid for each condition.* **(C)** *Raster plots of z-scored calcium transients in the same animal under different conditions. Traces are sorted by similarity.* **(D)** *Violin plots quantifying the number (left), amplitude (middle), and decay (right) of detected calcium transients. White dots indicate median, vertical thick and thin lines indicate 1ˢᵗ-3ʳᵈ quartile and interquartile range, respectively.* **(E)** *tSNE plot summarizing the average calcium transients properties. Each data point represents one recording session. Asterisks in (D) indicate significant differences to wakefulness. *** p < 0.001. Note, to facilitate readability, only differences to wakefulness are indicated. For full report of statistics, see statistics table.*

9

Iso, Keta/Xyl and MMF distinctly modulate cellular calcium dynamics in individual neurons

One possible explanation for these distinct modes of calcium activity could be that each anesthetic condition recruits a unique set of neurons characterized by particular spiking properties. We tested this possibility by analyzing calcium transients in neurons that were active during all conditions (Fig. 4A, S5, S6). To obtain a sufficient number of active neurons, we extracted calcium transients using a lower quality threshold, accepting more neurons per recording (see Methods). In this manner, we obtained a median of 783 neurons per recording (min-max of 156-1641). While this shifted the overall distribution of calcium parameters to lower values, the relative ratios between the four conditions remained the same and the differences between anesthesia groups were preserved (Fig. S3F-G). Also, when considering only neurons that were active in all four conditions, rate as well as amplitude of calcium peaks were generally reduced under anesthesia, being lowest in the Keta/Xyl condition (Fig. 4B,C). Compared to the whole dataset, differences in decay constant were less pronounced. The median decay constant strongly decreased for awake and MMF conditions, while it increased for Iso and Keta/Xyl. These results indicate that both the between- as well as the within-condition variance strongly decreased when considering only neurons active under all conditions.

The relatively low number of neurons active in all four conditions (335 neurons) limited the statistical analysis. Therefore, we compared neurons that were active in any two combinations of conditions (Fig. S6C). This analysis further corroborated the similarity of neurons active during wakefulness and Iso anesthesia (Fig. 4C, S6C). Rate, amplitude, and duration of calcium transients were most similar between wakefulness and Iso compared to the other GAs. In contrast, neurons active during wakefulness and either Keta/Xyl or MMF showed decreased rate, amplitude and duration under anesthesia, with Keta/Xyl causing the strongest phenotype (Fig S6C). Overall, this indicates that anesthetics influence the firing properties of hippocampal neurons. However, the magnitude and direction of these effects vary considerably. Iso anesthesia has the mildest effect, and it most likely arises from distinct neuronal populations being active in the two conditions (wakefulness vs. Iso anesthesia), as the firing properties of cells that are active in both are barely affected (Fig. 4B,C). On the other hand, the strong effects of MMF and Keta/Xyl on all calcium parameters in the same cells indicate that different anesthetics directly alter the firing properties of individual neurons. Thus, alterations in firing properties of neuronal populations (e.g., SUA, Fig. 2B-D) are not solely explainable by different subpopulations of neurons being active between awake and anesthesia.

10

349
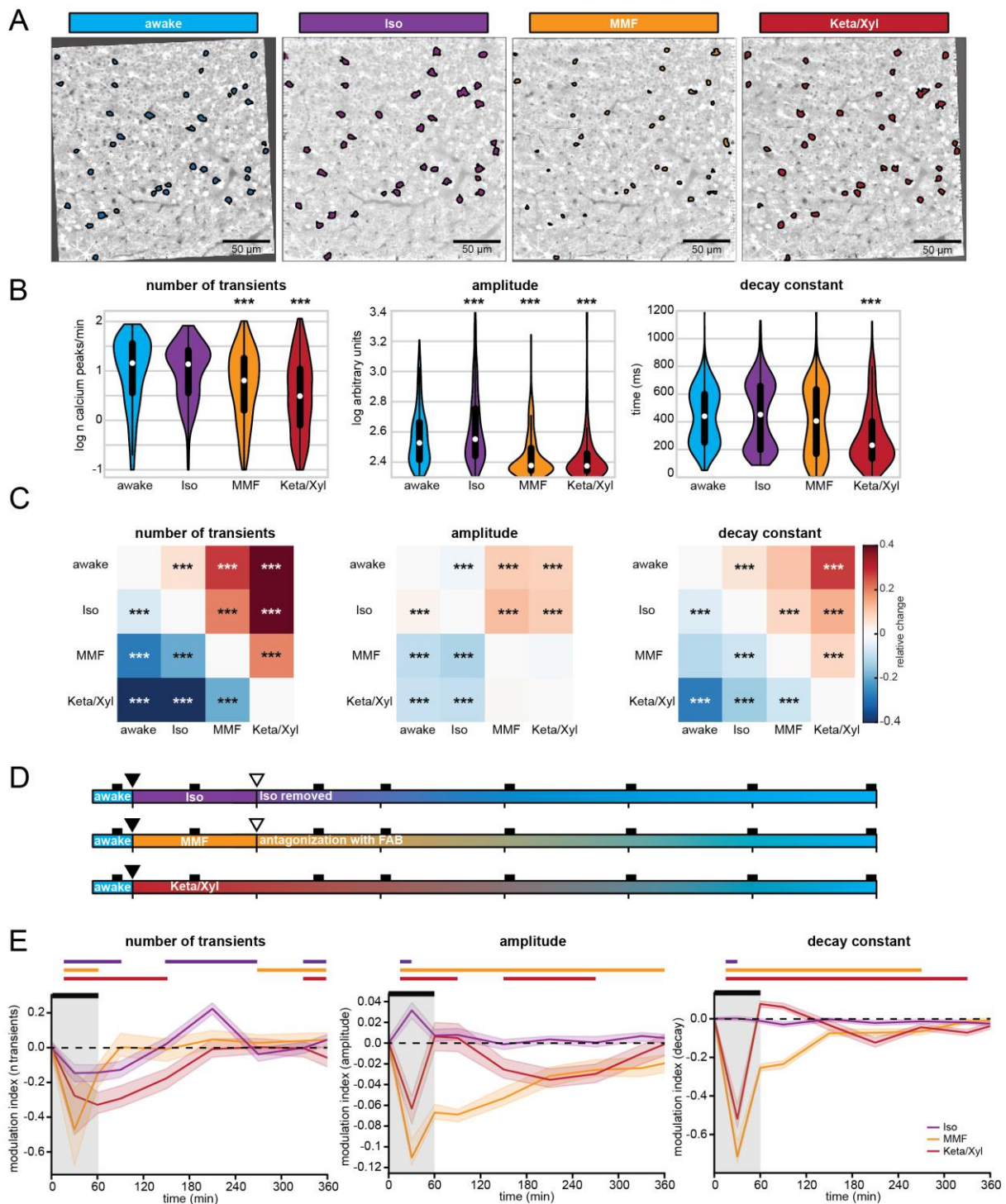
Figure 4: Calcium activity profiles in neurons active during all conditions are similar between wakefulness and Iso. (A) *Two-photon time-averaged images of the same FOV in CA1, aligned to the Iso condition (same images as in figs. 3). ROIs show neurons active in each condition, allowing direct comparison of calcium transients in the same cells under different conditions. **(B)** Violin plots quantifying the number (left), amplitude (middle), and decay (right) of detected calcium transients. White dots indicate median, vertical thick and thin lines indicate 1st-3rd quartile and interquartile range, respectively. **(C)** Heat maps displaying the relative change in the number (left), amplitude (middle), and decay (right) of calcium transients between neurons active in pairs of conditions (see also Fig. S6C). **(D)** Schematic representation of long-term calcium imaging experiments to assess recovery from anesthesia. Black rectangles indicate imaging time points (up to 10 min duration each). Filled and open triangles indicate the start and end of the anesthesia period. **(E)** Line diagrams showing the relative change (modulation*

11

361 *index) of the median number of calcium transients (left), their amplitude (middle), and decay constant*
362 *(right) during anesthesia and recovery relative to the awake state before anesthesia induction. The black*
363 *bar indicates the anesthesia period. Shaded, colored lines indicate 95% confidence interval. Note,*
364 *Keta/Xyl anesthesia could not be terminated. The horizontal, colored lines indicate significant difference*
365 *(p < 0.05) to awake time point (t = 0) for the respective condition. Asterisks in (B) and (C) indicate*
366 *significant differences to wakefulness. *** p < 0.001. Note, to facilitate readability, only differences to*
367 *wakefulness are indicated. For full report of statistics, see statistics table.*

368

369 **Population activity recovers with different temporal dynamics after Iso, Keta/Xyl and**
370 **MMF**

371 The LFP recordings showed that network activity remained altered for 1.5 h after Keta/Xyl
372 injection, but also after antagonization of MMF, while most aspects returned to pre-anesthetic
373 conditions during 45 min after Iso removal. To assess network effects of the different
374 anesthetics on a longer time scale, we used repeated calcium imaging during 6 hours after
375 anesthesia onset and 5 hours after Iso termination and MMF antagonization (Fig. 4D). In line
376 with our previous results, the number of calcium transients was strongly reduced 30 min after
377 MMF or Keta/Xyl injection, while the reduction had a lower magnitude for Iso. Similarly, MMF
378 and Keta/Xyl most strongly reduced the amplitude and duration of calcium transients, while Iso
379 mildly increased amplitude without affecting the decay constant (Fig. 4E).

380 Confirming the action dynamics monitored by LFP recordings in vivo, recovery from Iso
381 anesthesia was fast and only the rate of transients mildly changed during the hours after
382 removing the mask. In contrast, after Keta/Xyl injection, amplitude and duration of transients
383 were altered throughout the following 6 hours, while the reduction of the calcium transients
384 rate was not reverted until up to 4 hours later. Recovery to the pre-anesthetic state was even
385 slower after MMF/FAB. Despite antagonization of MMF anesthesia with FAB, calcium
386 transients remained disturbed for up to 6 hours. Thus, the different anesthetics not only induce
387 unique alterations of CA1 network dynamics, but also show different recovery profiles (Fig.
388 S6E).

389 **Anesthesia decorrelates hippocampal activity**

390 Calcium imaging studies in the visual cortex of ketamine anesthetized rats [27] and Iso
391 anesthetized mice [25] showed that anesthesia increases the overall pairwise correlations
392 between firing neurons and, consequently, induces more structured patterns of activity. While
393 neocortical L2/3 cells typically show a high degree of local interconnectivity [47], this is not the
394 case for CA1, where pyramidal cells receive their main excitatory input from CA3 and
395 entorhinal cortex and send their efferents to subiculum and extrahippocampal areas [9].
396 Another difference between neocortex and hippocampal CA1 area is that the neocortex
397 receives strong direct input from primary thalamus, which is a major source for slow oscillations
398 during anesthesia-induced unconsciousness and sleep [1, 48, 49]. In comparison to neocortex,
399 hippocampus shows different patterns of activity, including sharp waves, which are generated
400 intrinsically in the hippocampus, likely originating in CA3 [50]. To investigate whether these
401 differences cause a different impact of anesthesia on the population activity in CA1 when
402 compared to the neocortex, we analyzed the dynamical structure of population activity using
403 both calcium imaging and SUA of extracellular recordings in vivo. First, we analyzed Fisher-
404 corrected Pearson pairwise correlation between neuropil-corrected raw fluorescence traces.
405 We found that both correlation and anticorrelation were highest in animals during quiet
406 wakefulness (Fig 5A-B). In particular, the awake condition had a higher proportion of

407 correlation coefficients both in the 1st as well as in the 4th quartile of the entire distribution and,
408 accordingly, higher absolute correlation values (Fig. 5B, S7A). Similar to the firing properties
409 (SUA, fig. 2), Iso induced the milder changes, whereas Keta/Xyl caused the strongest
410 phenotype. This relationship was preserved in neurons active during all conditions (Fig. S7B),
411 indicating that anesthesia generally reduces correlated activity between neurons and that this
412 effect is not attributable to the activity of particular neuronal subpopulations. Moreover, these
413 effects were not influenced by the distance between the pair of neurons whose correlation was
414 quantified (Fig. 5C). These findings highlight the major differences between the anesthesia-
415 induced effects on neuronal coupling in hippocampal CA1 and neocortex. In accordance with
416 the anatomy of CA1, the correlation between pairs of neurons was only mildly affected by the
417 distance between them, with or without anesthesia. Not only were neurons less highly
418 correlated to each other under anesthesia, but their coupling to the whole population activity
419 [51] was reduced as well. The proportion of neurons with population coupling in the 4th quartile
420 of the entire distribution was highest for awake, and most strongly reduced under Keta/Xyl and
421 MMF, while Iso showed only mild effects (Fig. 5D).

422 To further relate the calcium imaging data to extracellular recordings of neuronal firing, we
423 carried out an analogous analysis on SUA. To avoid the confounding effect of firing rate, we
424 quantified the correlation between pairs of neurons using the spike-time tiling coefficient [52],
425 a measure that is largely insensitive to variations of the firing rate (see Methods). To be
426 consistent with the calcium data, we quantified correlations within 1 second, a timescale of the
427 same magnitude as the decay constant used to extract calcium signals (700 ms). This analysis
428 confirmed that all anesthetics decorrelated neuronal activity (Fig. 5E). This effect was still
429 present, albeit less pronounced, using an integration window of 10 ms, which is closer to the
430 duration of action potentials (Fig. S7C). Overall, the decorrelation was milder under Iso
431 anesthesia and stronger under Keta/Xyl and MMF. Thus, all three GAs decorrelated calcium
432 transients and spiking activity in the CA1 area, with MMF and Keta/Xyl inducing the most
433 prominent effects.

434
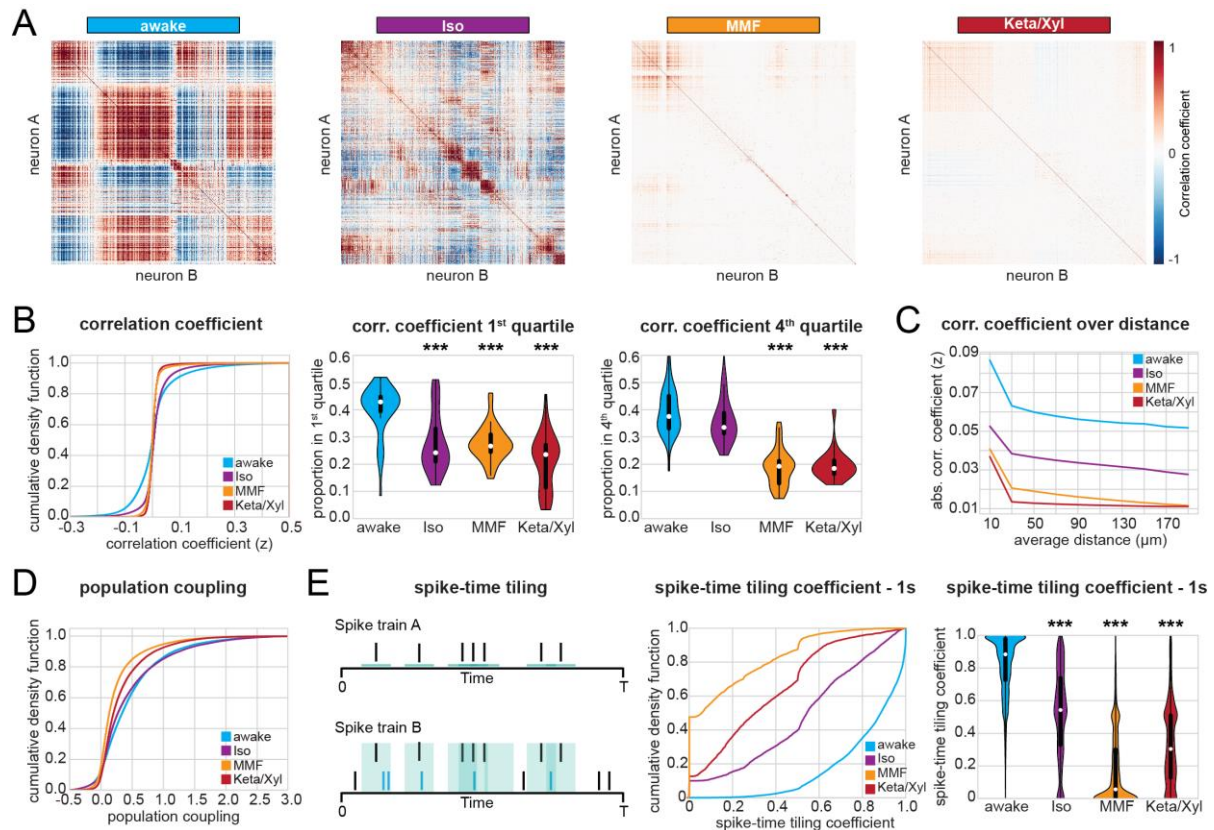
Fig. 5. Correlation analysis of CA1 calcium activity and SUA shows decorrelation under anesthesia. (A) *Heat maps displaying representative correlation matrices of calcium activity between pairs of neurons during wakefulness and the three different anesthetic conditions in the same animal. Matrices are sorted by similarity.* **(B)** *Left: Line plot displaying cumulative distribution of Fisher-corrected Pearson correlation coefficients between pairs of neurons (calcium imaging). Center: violin plot displaying the proportion of pairs found in the 1st (most negative) and 4th (most positive) quartile of the distribution.* **(C)** *Line plot displaying the absolute pairwise correlation coefficients over distance (calcium imaging, 25 micrometer bins).* **(D)** *Line plot displaying the cumulative distribution of population coupling (calcium imaging).* **(E)** *Quantification of correlation between pairs of extracellularly recorded single units using the spike-time tiling coefficient (STTC). Left: Schematic illustration of the STTC quantification. Center: cumulative distribution of the STTC with a 1000 ms integration window. Right: violin plot quantifying the STTC. In violin plots, white dots indicate median, vertical thick and thin lines indicate 1st-3rd quartile and interquartile range, respectively. Asterisks in (B) and (E) indicate significant differences to wakefulness. *** $p < 0.001$. Note, only differences to wakefulness are indicated. For comparison between conditions, see statistics table.*
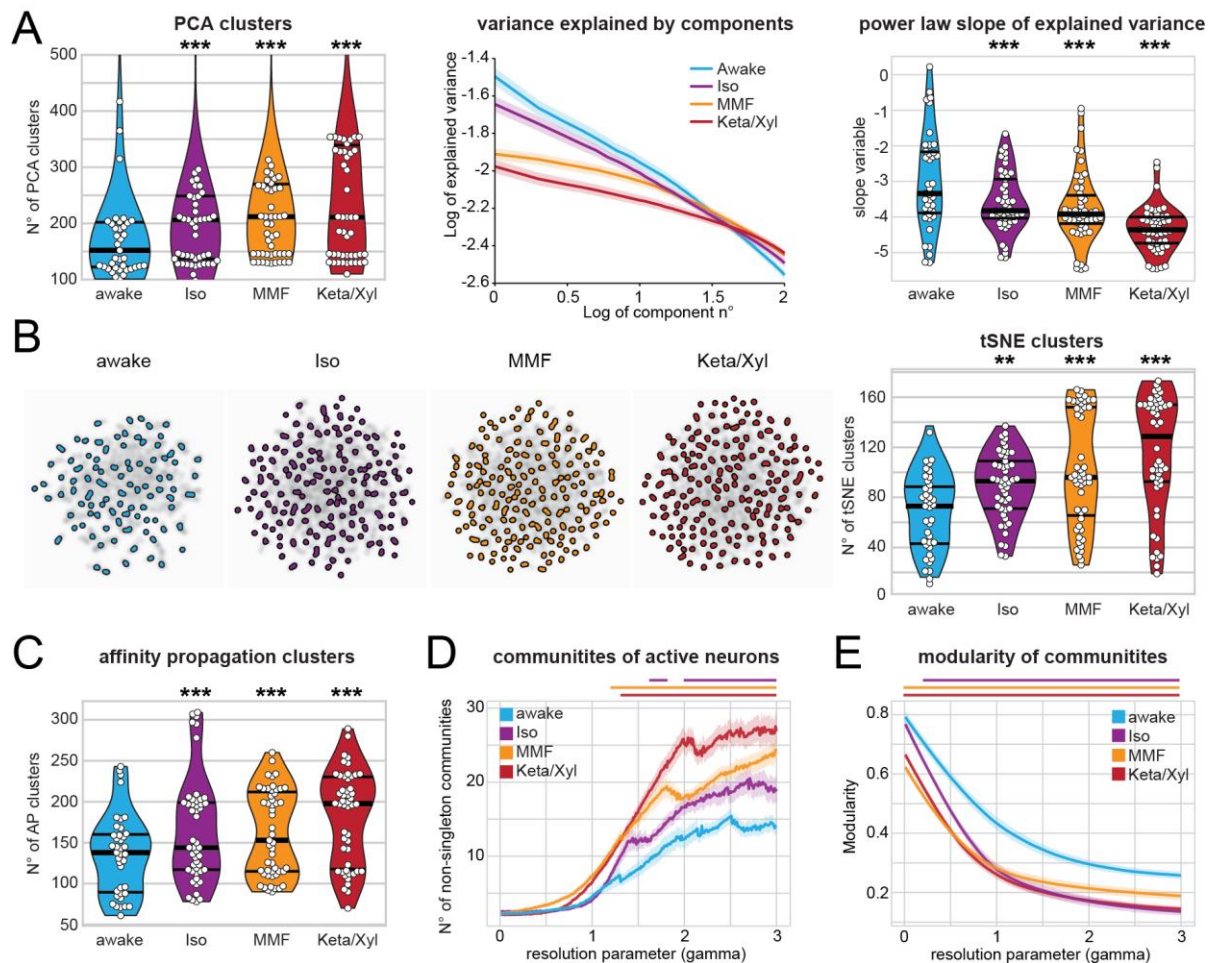
Anesthesia fragments temporal and spatial structure of hippocampal activity

The decorrelation of neuronal activity during anesthesia suggests that GAs might impact the spatial and temporal organization of CA1 neuronal ensembles (see Fig. 5A). To test this hypothesis, we analyzed the same number of active neurons for each condition, since a different number of neurons in each condition potentially influences the number and size of detected clusters [26]. First, we monitored the impact of GAs on the temporal structure of CA1 activity. We defined the number of clusters identified by principal component analysis (PCA) as the number of components that were needed to explain 90% of the variance. Moreover, we assessed the power-law slope of variance explained over the first 150 components (Fig. 6A). Both methods led to a larger number of clusters and a flatter power-law slope for anesthesia

14

462   when compared to wakefulness (Fig. 6A). Further corroborating these findings, both tSNE
463   dimensionality reduction and affinity propagation (AP) clustering (see Methods) also revealed
464   a larger number of clusters for anesthesia compared to wakefulness (Fig. 6B,C). These
465   observations indicate that activity is less structured under anesthesia. In line with previous
466   results, Iso had the weakest effect, whereas Keta/Xyl consistently induced the most
467   pronounced phenotype. Analysis of the deconvolved calcium traces led to comparable results
468   (Fig S8A,B). These findings support the idea that GAs fragment the hippocampal network into
469   a more diverse repertoire of microstates.

470   Second, we tested whether anesthesia disrupted the spatial structure of hippocampal activity,
471   employing a modularity maximization approach [53, 54] designed to detect internally densely
472   connected communities (modules). To allow detection of modules at varying sizes, we carried
473   out our analysis while varying a resolution parameter (gamma) and thus focusing on different
474   spatial scales. Using this approach, we showed that GAs increase the number of detected
475   communities over a wide range of resolution parameter values (Fig 6D). Moreover, the
476   modularity of these communities was lower than in wakefulness (Fig 6E). These results
477   indicate that anesthesia results in a more fractured network with, on average, smaller and less
478   coherent communities. A multi-resolution approach [55] followed by the selection of partitions
479   based on hierarchical consensus clustering yielded similar results (Fig. S8C). Among GAs, Iso
480   induced the mildest phenotype, whereas Keta/Xyl had the most prominent effects. Thus, GAs
481   not only decorrelate hippocampal activity, but also consistently fragment both its temporal and
482   spatial structure.

483

Fig. 6. Calcium activity in CA1 is temporally and spatially fragmented during anesthesia. (A) *Left: violin plot quantifying the number of principal component analysis (PCA) clusters during wakefulness or anesthesia, as indicated. Middle: log-log line plot displaying the variance explained by the first 100 components for each condition. Right: violin plot quantifying the power-law slope of the variance explained by the first 100 components for each condition.* **(B)** *Left: tSNE plots of network events recorded in the same animal under the four indicated conditions. Right: Violin plot quantifying the number of tSNE clusters obtained from calcium recordings during the four different treatments.* **(C)** *Violin plot quantifying the number of clusters obtained by affinity propagation from calcium recordings during the four different treatments.* **(D)** *and* **(E)** *Line plots quantifying the number of detected communities and the modularity of the detected communities with the resolution parameter gamma ranging from 0 to 3. Horizontal lines in violin plots indicate median and 1st-3rd quartile. Asterisks in (A) - (C) indicate significant differences to wakefulness. ** p < 0.01, *** p < 0.001. Horizontal lines above plots in (D) - (E) indicate significant difference to wakefulness. Anesthetic conditions are color-coded. Note, only differences to wakefulness are indicated. For comparison between conditions, see statistics table.*

Network alterations during sleep are less pronounced compared to anesthesia

Altered CA1 activity under anesthesia may affect synaptic function and memory processing. A naturally-occurring form of unconsciousness is sleep, which is required for network processes involved in memory consolidation [49, 56]. To decide whether the network perturbations described above resemble those naturally occurring during sleep, we first monitored CA1 activity by recording the LFP and spiking together with animal motion and the neck-muscle electro-myogram (EMG) in head fixed mice (Fig. S9A). We classified the signal into 30 s-long epochs of wake, rapid-eye-movement (REM) and non-REM (NREM) sleep. Further, a certain

508 fraction of epochs, which we labelled as "uncertain", could not be reliably classified into any of
509 the previous three categories, (see Methods for details). Given that the behavioral attribution
510 of these epochs is uncertain and difficult to interpret, we excluded them from further analysis.
511 The animals spent most of their sleeping time in the NREM phase, with only short periods of
512 intermittent REM sleep (Fig. 7A,I). The LFP showed enhanced theta power during REM
513 phases, while the power at low frequencies was broadly increased during NREM sleep (Fig.
514 7B,C). Compared to anesthesia (Fig. 1), these changes in the LFP both during REM and
515 NREM phases were modest. Along the same line, 1/f slope during NREM and REM sleep
516 slightly decreased, indicating a small reduction of the E/I balance that had a significantly lower
517 magnitude than the perturbation induced by GAs (Fig. 1D). Furthermore, the SUA rate was
518 slightly reduced (Fig. 7E-F), in contrast to all anesthetics, that strongly suppressed firing (Fig.
519 2). As previously reported [44], and similarly to the effect of GAs, we detected a small but
520 significant negative correlation between the NREM-induced reduction of firing rate and the
521 wakefulness firing rate, whereas the effect failed to reach statistical significance for REM sleep
522 alone (Fig. 7G). Moreover, NREM sleep induced a small reduction of pairwise correlation
523 between pairs of neurons, as measured by the spike-time tiling coefficient with an integration
524 window of one second.

525 To additionally investigate the effect of sleep on hippocampal activity, we used the above-
526 mentioned recordings to train a machine-learning algorithm to classify wakefulness, NREM
527 and REM sleep from eye videography images alone (Fig. S9) [57] (see Methods for details).
528 In line with previous results, we were able to reliably distinguish wakefulness and NREM sleep
529 (4-fold cross-validation accuracy >85%), whereas REM classification was less precise (4-fold
530 cross-validation accuracy ~30%). This classifier was then used to predict the physiological
531 state of mice from which we recorded calcium transients in CA1 neurons. In the calcium
532 imaging dataset, sleep was dominated by the NREM phase and only 17 min of REM sleep
533 could be detected in a total of 864 min (Fig. 7I). Given the limited amount of detected REM
534 sleep, its effects on hippocampal calcium activity should be interpreted with caution. As
535 reported for LFP data, NREM only mildly reduced the rate of calcium transients, whereas REM
536 sleep induced a small increase. In contrast, both NREM and REM sleep caused a small
537 reduction in transient amplitude (Fig. 7K). Further, we did not detect an effect of the sleep
538 state on absolute pairwise correlations (Fig. 7L).

539 In conclusion, sleep and GAs similarly affect the CA1 activity. However, the magnitude of
540 effects was much smaller for sleep than for GAs. Both NREM and REM states were more
541 similar to wakefulness than to the anesthetic state. Compared to the three different anesthetics,
542 sleep had the closest resemblance to Iso. Thus, among the three different anesthetics, network
543 alterations under Iso deviate the least from natural states such as wakefulness and sleep.

17
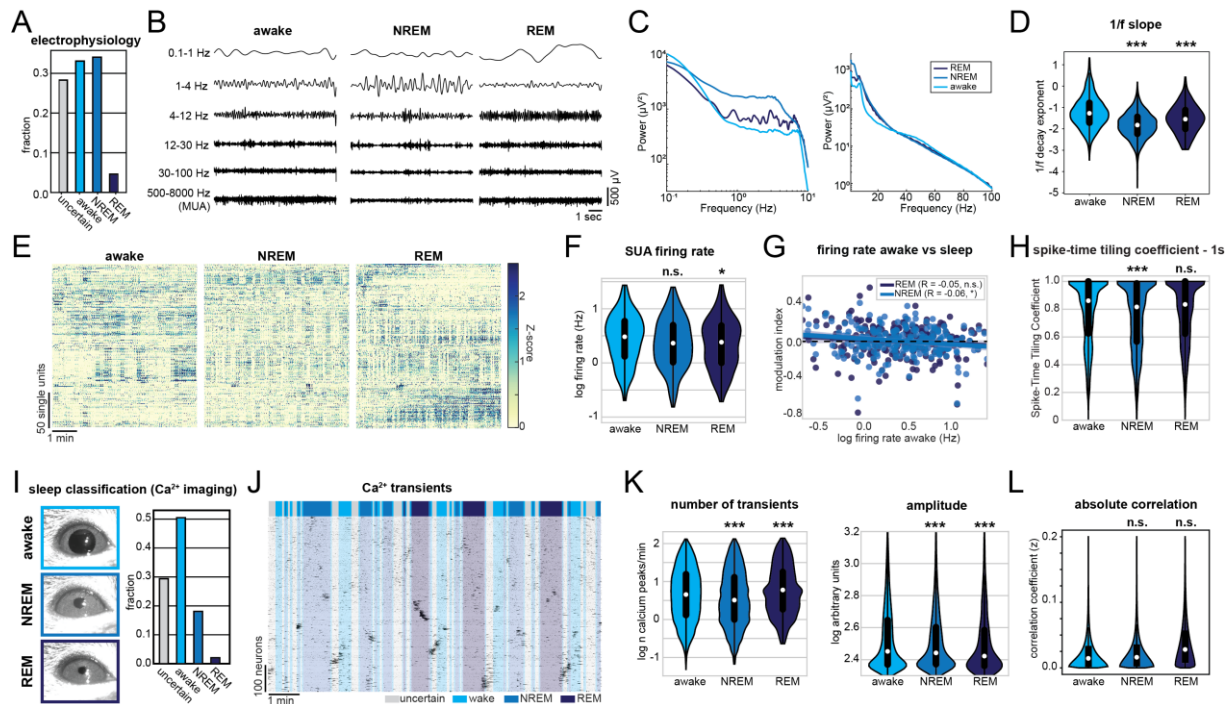
Fig. 7. Sleep alters CA1 activity in a similar way to anesthesia but with a lower magnitude. (A) Classification of activity states during electrical recordings. (B) Characteristic LFP recordings during wakefulness, NREM and REM sleep. (C) Line plot displaying LFP power spectra for the indicated activity states. (D) Violin plot displaying the power-law decay exponent (1/f) of the LFP power spectrum. (E) Raster plots of z-scored single-unit activity (SUA) for the three different activity states in four mice. Units are sorted according to initial activity during wakefulness. (F) Violin plot showing SUA firing rate. (G) Scatter plot showing modulation of SUA firing rate during NREM (light blue) and REM sleep (dark blue) with respect to activity during wakefulness. (H) Violin plot quantifying the STTC. (I) Classification of activity states during CA1 calcium imaging based on eye videography. (J) Raster plots of z-scored calcium transients in an example recording of one animal transiting between wakefulness and sleep. Traces are sorted by similarity. (K) Violin plots quantifying the number (left), and amplitude (right) of detected calcium transients. (L) Violin plots quantifying absolute pairwise correlation of all recorded neurons. White dots indicate median, vertical thick and thin lines indicate 1st-3rd quartile and interquartile range, respectively. * p < 0.05, ** p < 0.01, *** p < 0.001 w.r.t. to wake state, n = 3-7 mice.

Repeated anesthesia alters spine dynamics in CA1

The impact of Iso, MMF, and Keta/Xyl on CA1 activity might alter spine dynamics at CA1 pyramidal neurons. This issue is of critical relevance, since GAs disrupt activity patterns during development [58] also involving alteration of synaptic connectivity [59-61], but less is known about the impact of GAs on hippocampal synaptic structure during adulthood. So far, spine dynamics in hippocampus were only investigated under anesthesia, lacking comparison to the wake state. Moreover, the reported turnover rates varied strongly between studies [21, 62, 63]. Thus, it is unknown how repeated anesthesia in itself affects spine stability.

We repeatedly imaged the same basal, oblique, and tuft dendritic segments of CA1 pyramidal neurons under all four conditions (five times per condition, every four days), interrupted by a 30-day recovery period between conditions (Fig. 8A, S10A). To rule out time-effects, we pseudo-randomized the order of anesthetics (Fig. S10A). During wakefulness, without any anesthesia in between, the turnover ratio of spines on all dendrites was on average 18.6 - 20.5 % per four days. This turnover ratio was stable and did not change systematically over

18

574 successive imaging sessions (Fig. 8B). Notably, all anesthetics affected spine turnover. Both
575 MMF and Iso anesthesia mildly increased the turnover ratio compared to wakefulness (21.1 –
576 23.8 % for MMF, 24.0 – 24.7 % for Iso). Iso did not alter the surviving fraction of spines.
577 Together with the significant increase in spine density over time (Fig. 8B) these results indicate
578 that the elevated turnover ratio was due to a rise in the gained fraction of spines (Fig. S10B).
579 In contrast, MMF led to a slight increase in the fraction of lost spines (Fig. S10B) and
580 correspondingly, slightly decreased the surviving fraction compared to wakefulness. Spine
581 density did not change over time. Keta/Xyl anesthesia showed the strongest effect on spine
582 turnover (13.4 - 15.7 %), which was opposite to MMF and Iso, and therefore significantly lower
583 rather than higher compared to the awake condition (Fig. 8B). This lower turnover ratio was
584 accompanied by a higher surviving fraction and an increase in density with time (Fig. 8B).
585 Consistently, the fraction of lost spines was most strongly reduced (Fig. S10B). Thus, Keta/Xyl
586 anesthesia resulted in marked stabilization of existing spines and a reduction in the formation
587 of new spines, indicative of a significant effect on structural plasticity. These effects were
588 present on basal dendrites of stratum oriens (S.O.), oblique dendrites in stratum radiatum
589 (S.R.) and tuft dendrites in stratum lacunosum moleculare (S.L.M.), albeit with different
590 magnitude. Under Keta/Xyl the strongest impact on spine density was present in S.L.M., while
591 turnover was most strongly reduced in S.O. Also, the increased spine turnover seen under Iso
592 and MMF was most pronounced in S.O. (Fig. S10D).

593 To rule out that the age of the animal influenced spine dynamics in the awake condition, we
594 measured spine turnover in a group of age-matched animals to the first anesthesia group (Fig.
595 S10A,C). Moreover, to rule out that the chronic imaging procedure per se and anesthesia in
596 general had a long-lasting effect on the awake imaging condition, we added another awake-
597 imaging control group with naïve, age-matched animals to the awake imaging time point in the
598 experimental group (Fig. S10A,C). In all three groups, spine turnover was indistinguishable,
599 indicating that neither age nor previous imaging under anesthesia impacted spine dynamics in
600 the awake-imaging group (Fig. S10C).

601 Next, we asked whether the modulation of spine turnover by GAs was due to acute remodeling
602 of spines during the time of anesthesia. Alternatively, spine turnover might be driven by long-
603 lasting changes in network activity imposed by the slow reversal of all GAs. To capture fast
604 events such as filopodia formation, we acquired image stacks every 10 min (Fig. 8C). Spine
605 turnover, survival, or density were not significantly altered during the one hour of imaging (Fig.
606 8D). Thus, spines were stable during the one hour irrespective of the treatment. While mature
607 spines typically show low elimination/formation rates over one hour, filopodia are more
608 dynamic [64-66]. Unlike other reports, that observed an acute selective formation of filopodia
609 under Keta/Xyl, but not Iso [67], we did not detect any acute effects of GAs on filopodia turnover
610 of CA1 pyramidal cell dendrites. Thus, chronic exposure to all GAs consistently impacted spine
611 dynamics, whereas acute effects were lacking. Keta/Xyl caused a strong decrease in spine
612 turnover, accompanied by a higher surviving fraction and an increased density over time.

19
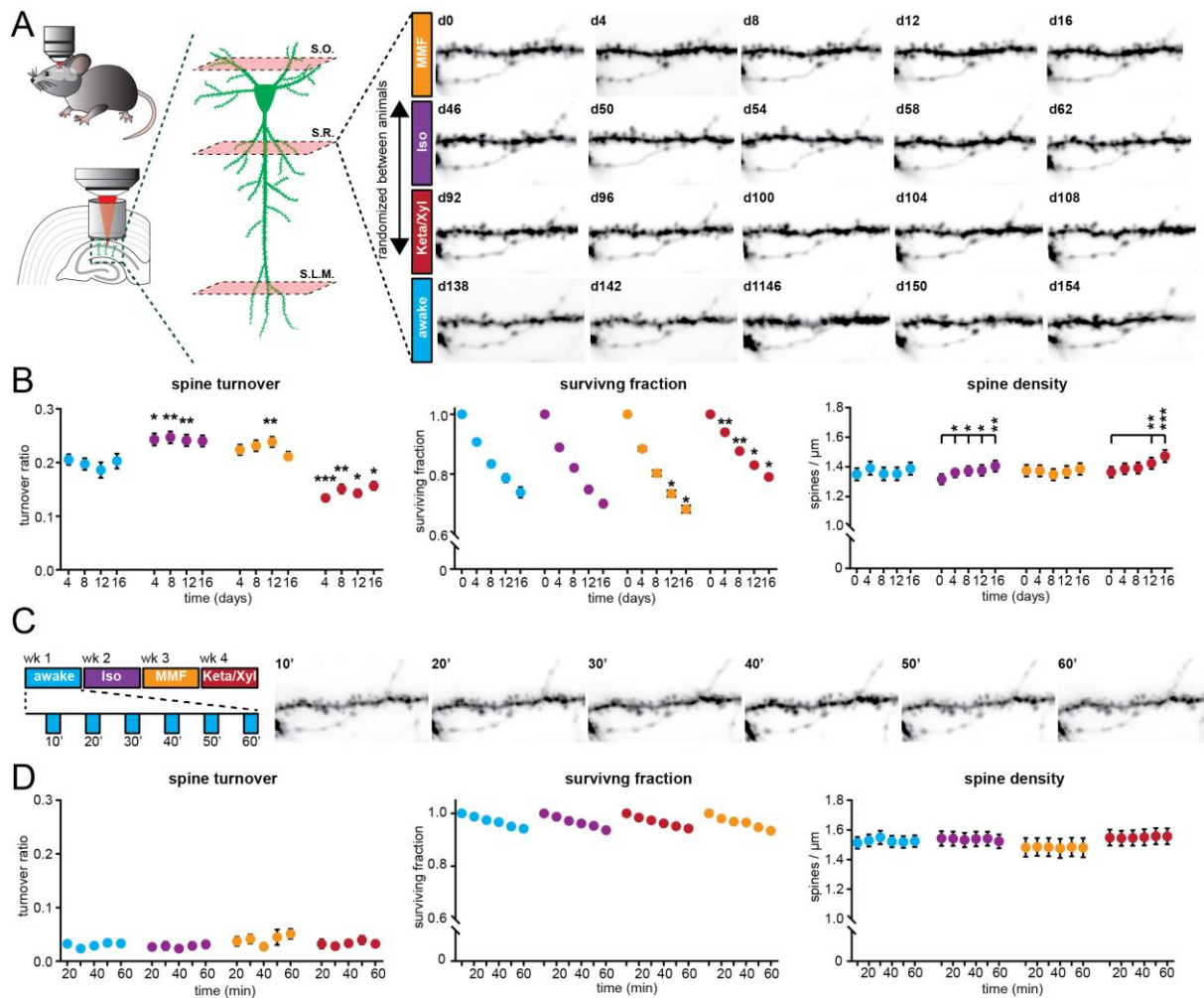
Fig. 8. Spine turnover at CA1 pyramidal neurons is distinctly altered by repeated application of Iso, MMF and Keta/Xyl. (A) Left: Schematic illustration of in vivo spine imaging strategy. In each animal, spines were imaged on basal dendrites located in stratum oriens (S.O.), oblique dendrites in stratum radiatum (S.R.) and tuft dendrites in stratum lacunosum moleculare (S.L.M.). Right: Example showing an oblique dendrite in S.R. imaged chronically during all conditions. The order of anesthetic treatments was pseudo-randomized between mice (see Fig. S10A). **(B)** Dot plots showing quantification of spine turnover (left), spine survival (middle) and spine density (right) under the four indicated treatments. Note that spines were imaged on the same dendrites across all conditions. Dots indicate mean ± SEM. Asterisks indicate significant differences to wakefulness in the left and middle panel. In the right panel, asterisks denote significant changes within each treatment compared to day 0. * $p < 0.05$, ** $p < 0.01$, *** $p < 0.001$. **(C)** Imaging of acute spine dynamics during four different conditions. Left: schematic of the experimental timeline. Right: example of dendrite imaged during wakefulness in 10 min intervals (same dendrite as in A). **(D)** Dot plots showing quantification of acute spine turnover (left), spine survival (center) and spine density (right) under the four indicated treatments. Dots indicate mean ± SEM.

Episodic memory consolidation is impaired by MMF and Keta/Xyl, but not by Iso

Episodic memory formation and consolidation require hippocampal activity. Newly learned experiences are thought of being consolidated via replay events that co-occur with low-frequency oscillations [49, 68-70]. In the hippocampus, these low-frequency events typically occur as sharp waves [50] during sleep, but also during awake resting behavior [70]. The above results from electrophysiological recordings and imaging showed that GAs strongly altered network oscillations in the CA1 area, in the case of MMF and Keta/Xyl, also long after

20

636 anesthesia discontinuation. Spine turnover of CA1 pyramidal neurons was also affected,
637 especially after Keta/Xyl administration. Therefore, we tested whether inducing anesthesia
638 shortly after the acquisition of a new episodic memory affected its consolidation (Fig. 9A). In
639 line with previous experiments, we restricted Iso and MMF anesthesia to one hour, while
640 Keta/Xyl anesthesia was left to recede spontaneously. We assessed episodic-like memory with
641 a water maze protocol for reversal learning, when the hidden platform was moved to the
642 quadrant opposite the initial target location (Fig. 9A). Specifically, we tested the effects of the
643 different anesthetics on the consolidation of the memory of the new platform location. We
644 compared the performance of the mice during the probe trial done on day 3 immediately after
645 the reversal learning protocol (and 30 min before anesthesia), with the performance during the
646 probe trial on day 4, twenty-four-hours after anesthesia. During the probe trial on day 3,
647 animals of all four groups spent significantly more time in the new target quadrant compared
648 to chance (25 %), indicating that they learned the new platform position successfully (Fig.
649 9B,C).

650 On day 4, control animals that did not undergo anesthesia showed the same performance as
651 on day 3, suggesting that they had retained the memory of the new platform location (Fig.
652 9B,C). However, animals that were anesthetized with Keta/Xyl or MMF spent significantly less
653 time in the new target quadrant and showed a significantly larger mean distance to the target
654 platform position compared to the probe trial on day 3. In the Iso group, no significant difference
655 compared to day 3 was detectable (Fig. 9B,C, S11A). The impairment of memory consolidation
656 was not explained by the longer duration of recovery after Keta/Xyl or MMF compared to Iso,
657 because anesthesia for up to 4 h with Iso had no disruptive effect (Fig. S11B,C). Thus, it is not
658 the duration of the induced unconsciousness but rather the type of anesthetic that likely
659 explains the impaired memory consolidation. Notably, the effects were relatively mild, and the
660 decrease in performance on day 4 was not significantly different between treatment groups. In
661 summary, consistent with long-lasting effects on CA1 network activity, Keta/Xyl, and MMF
662 impaired episodic-like memory consolidation. In contrast, Iso, which overall caused a weaker
663 disturbance of neuronal population activity and a faster recovery profile, did not significantly
664 affect memory consolidation.
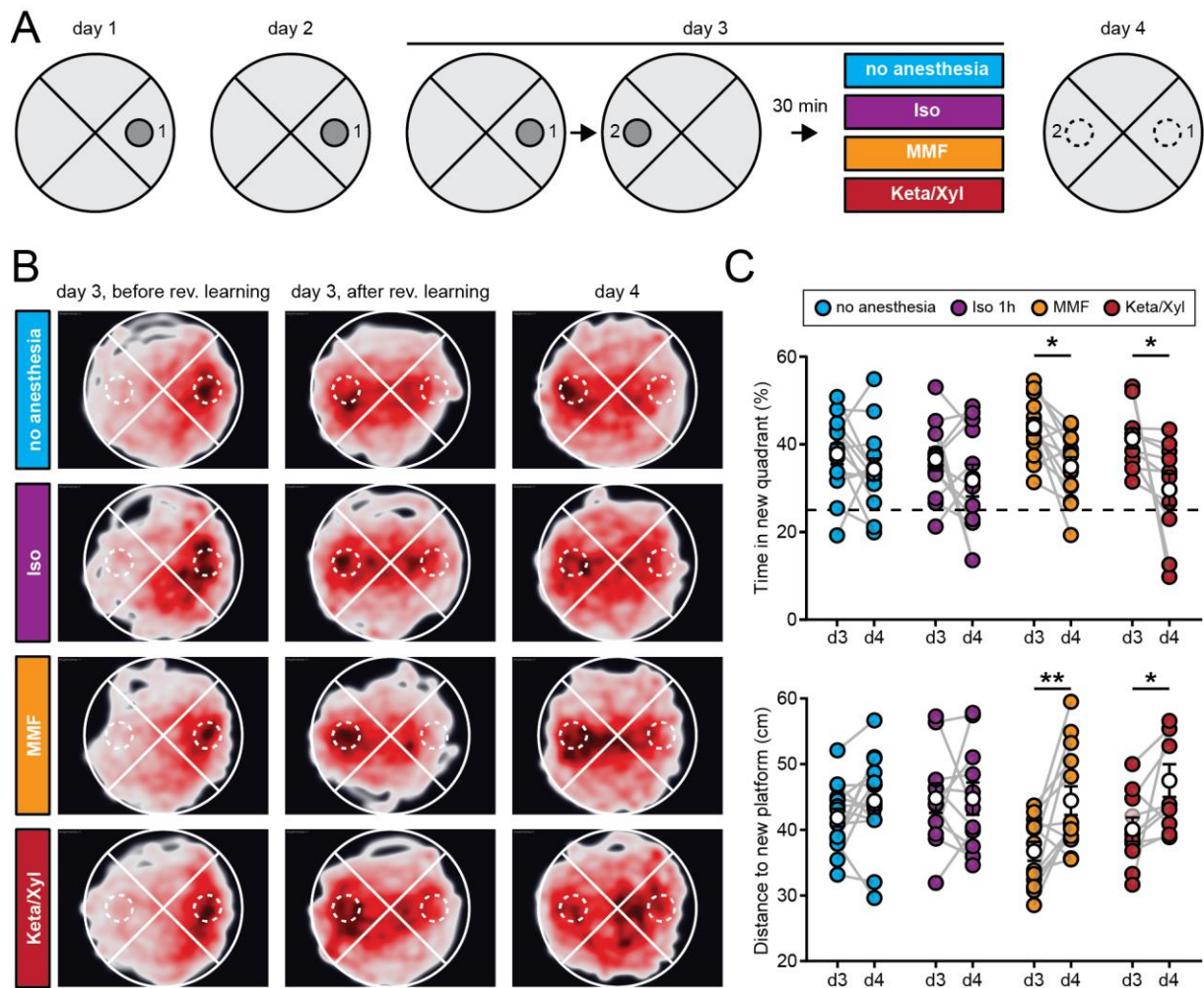
Fig. 9. Episodic memory consolidation is impaired by MMF and Keta/Xyl, but not by Iso. (A)
Experimental design to test episodic-like memory in a Morris water maze. On days 1 and 2, animals
were trained to find the platform in position 1. Reversal learning was performed on day 3 where animals
had to learn that the platform was moved to position 2. The training was followed 30 min later by a 1-h
period of one of the four indicated treatments per group. On day 4, consolidation of the memory for the
*platform in position 2 was tested. **(B)** Heat maps showing trajectories of all mice during the first probe*
trial before reversal learning on day 3 (left column), after reversal learning on day 3 (middle column) and
after treatment on day 4 (right column). The position of the target zone is indicated by dashed circles.
***(C)** Scatter plots showing quantification of time spent in the new target quadrant (top) and distance to*
the new platform (bottom) after reversal learning on day 3 and on day 4. Filled, colored circles indicate
individual animals, white circles indicate mean ± SEM. Asterisks in (C) indicate significant differences
*between days. * $p < 0.05$, ** $p < 0.01$.*

DISCUSSION

We investigated and systematically compared the intra- and post-anesthetic effects of different commonly used anesthetic strategies on the mouse hippocampus across multiple levels of analysis. Despite sharing some common traits, brain and cellular network states differ substantially under the influence of various types of anesthetics [30, 71, 72]. Indeed, at the neuronal level, compared with awake state and natural sleep, all three anesthetics showed robustly reduced spiking activity in single neurons, reduced power in the high oscillation frequency band, and decorrelated cellular population activity. However, the induced network

22

687 states in CA1 were highly distinct between the three different conditions, with Iso leading to
688 prominent network oscillations at around 0.1 Hz, which timed the spiking activity of single units
689 and neuronal calcium transients. Keta/Xyl caused pronounced oscillations between 0.5 and 4
690 Hz and the strongest reduction in calcium dynamics. MMF, in contrast, most strongly reduced
691 LFP and SUA and impaired population dynamics for many hours as assessed with calcium
692 imaging. Differences were also present in the long-term effects on spine dynamics, with
693 Keta/Xyl stabilizing spines, leading to reduced turnover and increased density. MMF, on the
694 other hand, mildly increased spine dynamics. Keta/Xyl cannot be antagonized and therefore
695 changes of the CA1 network mediated by this anesthetic were present hours after the injection,
696 in agreement with long-lasting overall changes of global animal physiology [38]. More
697 unexpectedly, and in contrast to overall effects on physiology [38], CA1 network dynamics
698 were still disturbed for at least 6 hours after antagonization of MMF anesthesia. These long-
699 lasting alterations were associated with impairment of episodic memory consolidation after
700 exposure to Keta/Xyl- or MMF, but not Iso. Thus, despite all fulfilling the same hallmarks of
701 general anesthesia, different GAs distinctly alter hippocampal network dynamics, synaptic
702 connectivity, and memory consolidation.

703 **Iso, MMF and Keta/Xyl have different molecular targets and distinctly modulate**
704 **functional and structural features of CA1**

705 The GAs used here represent three different strategies based on the large repertoire of
706 currently available anesthetics. Isoflurane represents the class of halogenated diethyl ether
707 analogues, which are volatile and therefore administered via inhalation. Fentanyl, in
708 combination with the analgesic medetomidine and the sedative midazolam (MMF), represents
709 an anesthetic approach based on the injection of a combination of drugs with sedative,
710 analgesic and anxiolytic properties. In the clinic, propofol can be used instead of midazolam.
711 Finally, ketamine is used both as an anesthetic and, at a lower dosage, as a treatment against
712 depression. For anesthesia, it is generally combined with xylazine, which acts as a sedative,
713 analgesic and muscle relaxant. All three strategies differ markedly in their molecular targets.
714 Consequently, they uniquely modulate general animal physiology [38] and brain activity [72].
715 Isoflurane is a potent GABA- and glycine receptor agonist. Moreover, it activates two-pore
716 potassium channels and acts as α-amino-3-hydroxy-5-methyl-4-isoxazolepropionic acid
717 receptor (AMPAR) inhibitor [4]. Similar to Iso, midazolam, the hypnotic component of the MMF
718 mix, mainly acts as a GABAR agonist with little effect on NMDARs. In contrast, ketamine is a
719 potent, use-dependent NMDAR blocker with less pronounced effects on potassium channels,
720 GABA, glycine and other glutamate receptors such as AMPA or kainite receptors [4]. Moreover,
721 while most anesthetics reduce the activity of thalamic nuclei, ketamine increases thalamic drive
722 [73], leading to enhanced rather than reduced oscillations in mid-to-high frequency bands such
723 as theta and gamma [28, 74]. In accordance with this, our study reveals major differences in
724 the action of the different anesthetics on functional and structural features of CA1. With both
725 electrical recordings and calcium imaging we report a robust reduction of neuronal spiking and
726 pairwise neuronal correlation. Notably, effects on electrical activity and calcium activity were
727 well in line for both Iso and MMF, despite the different recording methods. However, we
728 observed some divergence for Keta/Xyl.

729 **Comparison of electrophysiological recordings and calcium imaging**

730 Generally, differences in electrophysiological recordings and calcium imaging data may stem
731 from the location where the signal is detected. In the calcium imaging experiments, the signal
732 was sampled in a horizontal plane located inside and parallel to stratum pyramidale of CA1. In

733 this configuration, somatic, action-potential driven calcium transients mainly from pyramidal
734 neurons dominate the signal. Due to the kinetics and calcium-binding properties of GCaMP6f,
735 action potentials can only be resolved below approx. 5 Hz and are reported non-linearly [46,
736 75]. In contrast, the electrodes on linear probes are arranged orthogonally to the strata of CA1
737 and parallel to the dendrites of CA1 cells. Thus, synaptic potentials mainly constitute the LFP
738 across all layers and spikes are picked up from both pyramidal cells (in stratum pyramidale)
739 and GABAergic neurons in all layers. Moreover, the first method samples neurons that spatially
740 distribute over a large area. In contrast, the second one is biased towards large, active neurons
741 that are in close proximity of the electrode.

742 More specifically, under Keta/Xyl, the overall firing rate of single units showed the smallest
743 reduction of all three anesthetics. At the same time, imaging revealed the most substantial
744 reduction in rate, amplitude and duration of calcium transients (compare Fig. 2B and 3D). One
745 reason for this discrepancy may be the inhibitory action of ketamine on NMDARs. CA1
746 pyramidal cells display large, NMDAR-driven dendritic plateau potentials and calcium spikes
747 [76]. Moreover, ketamine likely inhibits L-type voltage-gated calcium channels [77] and
748 reduces burst firing [78], leading to calcium transients with reduced amplitude and a faster
749 decay constant. In contrast, ketamine has little influence on sodium spikes and AMPAR-
750 mediated synaptic potentials, which are detected in electrical recordings as SUA and LFP,
751 respectively. In accordance with electrical recordings, calcium transients showed increased
752 power at 0.1-0.2 Hz under Iso. However, we did not detect a clear peak at 1-4 Hz in the
753 presence of Keta/Xyl, as seen in LFP and SUA, probably due to its strongly dampening effect
754 on calcium transients. The (low-pass) filtering of neuronal activity imposed by calcium
755 indicators might also play a role [75].

756 Notably, the differences between electrical recordings and calcium imaging under Keta/Xyl are
757 relevant. Calcium is a second messenger central to neuronal plasticity and metabolism [79,
758 80]. NMDARs are a major source for activity-dependent calcium entry into the cell, involved in
759 regulating synaptic plasticity, metabolism, and pathology [81]. The present findings suggest
760 that Keta/Xyl has a particularly strong effect on neuronal calcium activity, uncoupling action
761 potential firing from associated cytosolic calcium transients, leading to reduced intracellular
762 calcium signaling. In contrast, calcium transients under MMF and Iso anesthesia closely
763 matched the electrical activity profile of neurons. Therefore, aside from overall effects on
764 network activity, Keta/Xyl may selectively alter neuronal plasticity by suppressing NMDAR-
765 dependent postsynaptic calcium signals.

766 **In contrast to neocortex, GAs decorrelate neuronal activity in CA1**

767 All anesthetics decorrelated neuronal activity in CA1, leading to an overall fragmented network
768 state with an increased number of temporal and spatial clusters. This is in stark contrast with
769 what has been reported from studies on GAs and cortical activity both at adulthood [25-27] and
770 during development [58]. This discrepancy may arise from the distinct architecture of CA1
771 compared to L2/3 of the neocortex, the latter showing a high degree of local interconnectivity
772 [47]. In CA1 this is not the case. Pyramidal cells receive their main excitatory input from CA3
773 and entorhinal cortex and send their efferents to subiculum and extrahippocampal areas
774 without making local connections among each other [9]. Afferent activity originating in various
775 sources and converging in CA1, may arrive out-of-phase under anesthesia, leading to
776 desynchronized firing of CA1 pyramidal cells. Such a phenomenon has been proposed as a
777 candidate mechanism underlying desynchronization of neuronal firing in basal ganglia under
778 conditions of slow oscillations (slow-wave sleep) and high synchrony in the neocortex [82].

779   Notably, the pairwise correlation was not entirely independent of the distance between
780   neurons. Synchronization of pyramidal neurons via local, GABAergic interneurons may be
781   another factor that increases spatial correlations. Both in the neocortex and hippocampus,
782   various types of GABAergic interneurons locally connect to and synchronize pyramidal
783   neurons such as basket or bistratified cells [83].

784   Coordinated neuronal network dynamics, including pairwise correlation of calcium transients
785   and single units, population coupling, clustering in the temporal and spatial domain were
786   consistently impaired most strongly with Keta/Xyl and MMF. Iso, both in electrophysiological
787   as well as calcium recordings, showed the mildest effects and permitted hippocampal activity
788   patterns that most closely resembled wakefulness and NREM/REM sleep. Iso and MMF, in
789   contrast to Keta/Xyl, are thought to be immediately reversible [38]. However, especially MMF
790   showed significant disruption of network dynamics long after reversal both in electrical
791   recordings and with calcium imaging. Antagonization of MMF failed to fully recover calcium
792   dynamics within the following 5 hours. Such long-lasting alterations might interfere with the
793   hippocampal function shortly after antagonization of MMF and must be considered when
794   performing whole-cell recordings in freely moving animals [84-86].

795   Since all anesthetics had a much longer effect on network activity than we expected, we asked
796   whether this is reflected in long-term effects of these different types of anesthetics on spine
797   dynamics of CA1 pyramidal neurons. Recent studies investigating spine dynamics at CA1
798   pyramidal neurons came to incongruent conclusions reporting spine turnover ranging from 3%
799   [63] over 12% [21] to approx. 80% [62] over 4 days. However, all studies used either isoflurane
800   [21] or ketamine/xylazine-based [62, 63] anesthesia during the repeated imaging sessions.
801   Thus, to what extent anesthesia itself influences spine dynamics is not clear.

802   **Iso, MMF and Keta/Xyl distinctly alter spine dynamics in CA1**

803   More generally, various effects of general anesthesia on spine dynamics were reported,
804   depending on the brain region, preparation, age of the animal and anesthetic strategy. For
805   example, enhanced synaptogenesis has been reported with different types of anesthetics on
806   cortical and hippocampal neurons during development [59, 60]. In contrast, one study indicated
807   that spine dynamics were not altered on cortical neurons of adult mice with Keta/Xyl or Iso
808   [67], while another study demonstrated an increase in spine density in somatosensory cortex
809   with ketamine [87]. Also, fentanyl-mediated, concentration-dependent bidirectional
810   modulations of spine dynamics were reported in hippocampal cultures [88].

811   To systematically compare spine dynamics in CA1 in vivo under different anesthetic
812   treatments, we imaged spines at basal, oblique and tuft dendrites in a large set of dendrites.
813   We found small, but robust chronic effects of repeated anesthesia. These alterations were
814   present in all strata of CA1, consistent with a layer-independent reduction of SUA during
815   anesthesia. Keta/Xyl decreased spine turnover leading to a mild increase in spine density over
816   time by stabilizing existing spines. This observation agrees with recent studies that showed a
817   stabilizing effect of ketamine in the somatosensory cortex, resulting in increased spine density
818   [87]. Thus, repeated anesthetic doses of Keta/Xyl may limit overall synaptic plasticity and thus
819   spine turnover. It was further shown that sub-anesthetic, antidepressant doses of ketamine
820   enhance spine density in the prefrontal cortex [89, 90], similar to our study of CA1 neurons.
821   Iso and MMF had contrasting effects on spine dynamics compared to Keta/Xyl, mildly
822   enhancing spine turnover, which might be explained by their different pharmacology compared
823   to ketamine, as pointed out above. A second aspect that distinguishes Keta/Xyl from Iso and
824   MMF is its irreversibility, which might lead to longer-lasting alterations of synaptic transmission

825 and E/I ratios leading to differential spine dynamics. This idea is supported by the observation
826 that during the anesthesia period itself, spine turnover was not altered, suggesting that long-
827 lasting and repeated disturbances are required to leave a mark in synaptic connectivity.

828 **MMF and Keta/Xyl, but not Iso, retrogradely affect episodic-like memory formation**

829 Sleep is a natural form of unconsciousness and is required for memory consolidation, including
830 hippocampus-dependent memories [49, 56]. Recent work suggested that sleep- and
831 anesthesia-promoting circuits differ [91, 92] while others identified circuit elements shared
832 between sleep and general anesthesia [93], especially during development [58]. Therefore, we
833 asked how the diverse alterations of CA1 network dynamics imposed by the different
834 anesthetics impact memory consolidation. In our study Iso resembled most closely network
835 states during wakefulness and natural sleep, while Keta/Xyl and MMF caused strong, lasting
836 alterations of LFP, SUA and calcium dynamics.

837 Notably, a single dose of anesthesia with Keta/Xyl and MMF, but not Iso disrupted memory
838 consolidation using a water maze assay in adult mice. Retrograde amnesia appeared to be
839 more sensitive to the magnitude than the duration of CA1 network disturbance imposed by the
840 various anesthetics. Keta/Xyl and MMF most strongly decorrelated CA1 network activity and
841 reverted only slowly. Extending the duration of Iso anesthesia up to 4 h, to match the slow
842 recovery after MMF and Keta/Xyl, did not affect memory consolidation. This observation
843 indicates that the slow recovery of network activity after Keta/Xyl and MMF alone cannot
844 explain anesthesia-mediated disruptions of memory consolidation. Instead, specific aspects of
845 the different anesthetics may selectively impact hippocampus-dependent memory formation.
846 For example, ketamine is an NMDAR blocker that has been shown to be necessary for the
847 long-term stabilization of place fields in CA1 [94], encoding of temporal information of episodes
848 [95], and formation of episodic-like memory [96].

849 Our results appear at odds with a report [97], where a single, 1-h treatment with Iso caused
850 deficits in the formation of contextual fear memory, object recognition memory and
851 performance in the Morris water maze in the following 48 h. However, this study investigated
852 memory acquisition after anesthesia (i.e., anterograde amnesia), while our study asked
853 whether anesthesia affects the consolidation of a memory formed shortly before the treatment
854 (i.e., retrograde amnesia).

855 Changes in synaptic connections are considered essential for memory formation and storage
856 [11-14]. Despite a small effect on spine dynamics, the strong and lasting disturbance of
857 hippocampal network activity in CA1 (and most likely other brain areas) by Keta/Xyl and MMF
858 was sufficient to interfere with memory consolidation. The chronic alterations of spine turnover,
859 especially by Keta/Xyl, may therefore indicate that repeated anesthesia can impact long-lasting
860 hippocampus-dependent memories.

861 To establish a direct link between spine dynamics, network disruptions and memory, future
862 studies are required that investigate both spine turnover and changes in population coupling
863 at hippocampal neurons causally involved in memory formation and maintenance.

864 Taken together, we report a novel effect of anesthesia on brain dynamics, namely
865 fragmentation of network activity in hippocampus. We consistently observe this phenomenon
866 across multiple levels of analysis. This unique response compared to the cortex may underlie
867 its high sensitivity to anesthesia, including its central role in amnesia. The extent, duration, and
868 reversibility of network fragmentation depend on the GA used. Therefore, this study may help
869 guide the choice of an appropriate anesthetic strategy, dependent on experimental

870   requirements and constraints, especially in the neurosciences. More generally, our findings
871   might also have relevance for the clinic. Postoperative delirium, a condition that involves
872   memory loss, is still an unresolved mystery. Minimizing the disturbance of hippocampal
873   function may be one building block to overcome this undesired condition.

874

AUTHOR CONTRIBUTIONS

	WY	MC	JAP	AF	AD	PP	CR	FM	OS	ILHO	JSW
Conceptualization	MAJOR	MAJOR	SUPPORT					SUPPORT	SUPPORT	SUPPORT	MAJOR
Investigation	MAJOR		MAJOR								
Data Curation	MAJOR	MAJOR	MAJOR	MAJOR	MAJOR						
Analysis	MAJOR	MAJOR	MAJOR	SUPPORT		SUPPORT		SUPPORT	SUPPORT		SUPPORT
Software		MAJOR	SUPPORT	MAJOR			SUPPORT		MAJOR		
Supervision								MAJOR	MAJOR	MAJOR	MAJOR
Funding acquisition	SUPPORT			SUPPORT						MAJOR	MAJOR
Project Administration										SUPPORT	MAJOR
Writing – original draft		MAJOR						SUPPORT			MAJOR
Writing – revisions	SUPPORT	SUPPORT	SUPPORT	SUPPORT						SUPPORT	MAJOR

LEVELS OF CONTRIBUTION: **MAJOR**, **SUPPORT**

ACKNOWLEDGEMENTS

DECLARATION OF INTERESTS

The authors declare no competing interests.

METHODS

Experimental Models and Methods

Mice

Adult C57BL/6J mice and transgenic Thy1-GFP-M mice of both sexes were housed and bred in pathogen-free conditions at the University Medical Center Hamburg-Eppendorf. The light/dark cycle was 12/12 h and the humidity and temperature were kept constant (40% relative humidity; 22°C). Food and water were available ad libitum. All procedures were performed in compliance with German law according and the guidelines of Directive 2010/63/EU. Protocols were approved by the Behörde für Gesundheit und Verbraucherschutz of the City of Hamburg.

Hippocampal recording-window surgery and in-vivo electrophysiology

Chronic multisite extracellular recordings were performed in dorsal CA1 during the dark phase of the dark/light cycle, except for sleep recordings, which were done during the light period. The adapter for head fixation was implanted at least 4 days before recordings. Mice were anesthetized via intraperitoneal injection of midazolam/medetomidine/fentanyl (MMF) and placed on a heating blanket to maintain the body temperature. Eyes were covered with eye ointment (Vidisic, Bausch + Lomb) to prevent drying. Prior to surgery, the depth of anesthesia and analgesia was evaluated with a toe-pinch to test the paw-withdrawal reflex. Subsequently, mice were fixed in a stereotactic frame, the fur was removed with a fine trimmer and the skin of the head was disinfected with Betaisodona. After removing the skin, 0.5% bupivacaine / 1%

907 lidocaine was locally applied to cutting edges. A metal head-post (Neurotar) was attached to
908 the skull with dental cement (Super Bond C&B, Sun Medical) and a craniotomy was performed
909 above the to the dorsal CA1 area (-2.0 mm AP, ± 1.3 mm ML relative to Bregma) which was
910 subsequently protected by a customized synthetic window filled with Kwik-Cast sealant (World
911 Precision Instruments). After recovery from anesthesia, mice were returned to their home cage
912 and were provided with Meloxicam mixed into soft food for 3 days. After recovery from the
913 surgery, mice were accustomed to head-fixation and trained to move in the Mobile HomeCage
914 system (Neurotar). For recordings, craniotomies were reopened by removal of the Kwik-Cast
915 sealant and multi-site electrodes (NeuroNexus, MI, USA) were inserted into the dorsal CA1
916 (one-shank, A1x16 recording sites, 50 μm spacing, 1.6 mm deep). A silver wire served as
917 ground and reference in the craniotomy between skull and brain tissue. Extracellular signals
918 were band-pass filtered (0.1-8000 Hz) and digitized (32 kHz) with a multichannel extracellular
919 amplifier (Digital Lynx SX; Neuralynx). The same animals were recorded weekly under different
920 anesthesia. After 15 min of non-anesthetized recording, mice received a subcutaneous
921 injection of Keta/Xyl, MMF or inhalation of Iso in a pseudo-randomized order. The following
922 drug combinations were administered: 2.0 % isoflurane in 100% O_2; 130 mg/kg ketamine, 10
923 mg/kg xylazine s.c.; 5.0 mg/kg midazolam, 0.2 mg/kg medetomidine and 0.05 mg/kg fentanyl
924 s.c.; and for complete reversal of anesthesia, 0.5 mg/kg flumazenil, 2.5 mg/kg atipamezole and
925 0.1 mg/kg buprenorphine s.c. Recordings were conducted for 1.5 h. After recordings, the
926 craniotomy was closed and mice were returned to their home cage. Electrode position was
927 confirmed in brain slices postmortem.

928 *EMG recordings*

929 Electromyography (EMG) electrodes for sleep state classification were implanted during
930 hippocampal recording-window surgery. Two gold plates (~3 mm diameter) soldered to epoxy
931 lacquered wires and attached to a connector were inserted into the right and left nuchal
932 muscles and fixed with dental cement (Super Bond C&B, Sun Medical). For EMG recordings,
933 a cable was attached to the implanted connector and directly digitized (32 kHz) and band-pass
934 filtered (8-8000 Hz) through a customized break-out channel board with a multichannel
935 amplifier (Digital Lynx SX; Neuralynx). EMG recordings were done at least for 1 h 45 min in
936 non-anesthetized mice without disturbances. Mice were recorded 1-2 times.

937 *Virus injection and hippocampal window surgery for in vivo calcium imaging*

938 C57BL/6J wild-type mice were anesthetized via intraperitoneal injection of
939 midazolam/medetomidine/fentanyl (MMF) and placed on a heating blanket to maintain the
940 body temperature. Eyes were covered with eye ointment (Vidisic, Bausch + Lomb) to prevent
941 drying. Prior to surgery, the depth of anesthesia and analgesia was evaluated with a toe-pinch
942 to test the paw-withdrawal reflex. Subsequently, mice were fixed in a stereotactic frame, the
943 fur was removed with a fine trimmer and the skin of the head was disinfected with Betaisodona.
944 The skin was removed by a midline scalp incision (1-3 cm), the skull was cleaned using a bone
945 scraper (Fine Science Tools) and a small hole was drilled with a dental drill (Foredom) above
946 the injection site. AAV2/7-syn-GCaMP6f was targeted unilaterally to the dorsal CA1 area (−
947 2.0 mm AP, ± 1.3 mm ML, − 1.5 mm DV relative to Bregma). 0.6 μl of virus suspension was
948 injected. All injections were done at 100 nl*min^{-1} using a glass micropipette. After the injection,
949 the pipette stayed in place for at least 5 min before it was withdrawn and the scalp was closed
950 with sutures. For complete reversal of anesthesia, mice received a subcutaneous dose of
951 Flumazenil, Atipamezole and Buprenorphine (FAB). During the two days following surgery
952 animals were provided with Meloxicam mixed into soft food. Two weeks after virus injection,
953 mice were anesthetized as described above to implant the hippocampal window. After fur

29

954 removal, skin above the frontal and parietal bones of the skull was removed by one horizontal
955 cut along basis of skull and two rostral cuts. The skull was cleaned after removal of the
956 periosteum, roughened with a bone scraper and covered with a thin layer of cyanoacrylate
957 glue (Pattex). After polymerization a 3-mm circle was marked on the right parietal bone
958 (anteroposterior, −2.2 mm; mediolateral, +1.8 mm relative to bregma) with a biopsy punch and
959 the bone was removed with a dental drill (Foredom). The dura and somatosensory cortex
960 above the hippocampus were carefully aspirated until the white matter tracts of the corpus
961 callosum became visible. The craniotomy was washed with sterile PBS and a custom-built
962 imaging window was inserted over the dorsal hippocampus. The window consisted of a hollow
963 glass cylinder (diameter: 3 mm, wall thickness: 0.1 mm, height: 1.8 mm) glued to a No. 1
964 coverslip (diameter: 3mm, thickness: 0.17 mm) on the bottom and to a stainless-steel rim on
965 the top with UV-curable glass glue (Norland NOA61). The steel rim and a head holder plate
966 (Luigs & Neumann) were fixed to the skull with cyanoacrylate gel (Pattex). After polymerization,
967 cranial window and head holder plate were covered with dental cement (Super Bond C&B,
968 Sun Medical) to provide strong bonding to the skull bone. Following the surgery, animals were
969 provided with Meloxicam mixed into soft food for 3 days. The position of the hippocampal
970 window was confirmed in brain slices postmortem.

971 *Two-photon calcium imaging in anesthetized and awake mice*

972 The same animals were sequentially imaged under Keta/Xyl, MMF or Iso in a pseudo-
973 randomized order during the dark phase of the dark/light cycle (for details, see above). After
974 losing the righting reflex, generally 5–10 min after application of the anesthetics, the animals
975 were positioned on a heating-pad to maintain body temperature at approximately 37°C during
976 anesthesia. The intensity of anesthesia and evaluation of the different stages of anesthesia
977 were assessed by recording the presence or absence of distinct reflex responses: righting
978 reflex, palpebral reflex, toe-pinch reflex. Between each imaging session, mice were allowed to
979 recover for one week.

980 Anesthetized mice were head-fixed under the microscope on a heated blanket to maintain
981 body temperature. Eyes were covered with eye ointment (Vidisic, Bausch + Lomb) to prevent
982 drying. The window was centered under the two-photon microscope (MOM-scope, Sutter
983 Instruments, modified by Rapp Optoelectronics) and GCaMP6f expression was verified in the
984 hippocampus using epi fluorescence. Images were acquired with a 16x water immersion
985 objective (Nikon CFI75 LWD 16X W, 0.80 NA, 3.0 mm WD). For awake imaging we used a
986 linear treadmill, which allowed imaging during quiet and running states. 5-min-timelapse
987 images were acquired every 10 minutes for a period of 50 minutes. Only quiet periods were
988 considered for analysis in this study. Image acquisition was carried out with a Ti:Sa laser
989 (Chameleon Vision-S, Coherent) tuned to 980 nm to excite GCaMP6f. Single planes (512x512
990 pixels) were acquired at 30 Hz with a resonant-galvanometric scanner at 29-60 mW (980 nm)
991 using ScanImage 2017b (Vidrio). Emitted photons were detected by a pair of photomultiplier
992 tubes (H7422P-40, Hamamatsu). A 560 DXCR dichroic mirror and a 525/50 emission filter
993 (Chroma Technology) was used to detect green fluorescence. Excitation light was blocked by
994 short-pass filters (ET700SP-2P, Chroma). For the repetitive imaging, the position of the field
995 of view (FOV) was registered in the first imaging session with the help of vascular landmarks
996 and cell bodies of CA1 pyramidal neurons. This allowed for subsequent retrieval of the FOV
997 for each mouse.

998 Calcium imaging experiments to measure recovery from anesthesia were done in five
999 additional animals. They were trained to maintain immobile on the treadmill for extended
1000 periods. We ensured to measure the same FOV and to maintain overall stability of

1001 fluorescence intensity for every recording in each imaging session for a given animal. The
1002 time-lapse recordings were extended to up to a maximum of 10 min per time point to have a
1003 higher probability of capturing motionless periods continuously, in awake and recovery states.
1004 Iso was applied for 60 min. FAB was injected 60 min after the application of MMF. Keta/Xyl
1005 was not antagonized. Imaging of calcium activity was performed before, 0.5, 1.5, 2, 3, 4, 5,
1006 and 6 hours after induction of anesthesia. For Iso and MMF, the 1.5 h time point represented
1007 the first imaging session after reversal. Untreated control animals were imaged every hour for
1008 the same amount of time.

1009 To habituate mice to sleep under head-fixation, we used a linear treadmill, which allowed the
1010 mice to move at will. Through the first 4 sessions mice were kept head-fixed for 15 to 30 min.
1011 In ten following sessions the fixation period was extended up to 4h with increasing intervals of
1012 30 min. The state of the mouse was continuously monitored with a USB camera and the
1013 running speed was recorded with custom-written scripts in the Matlab. After habituation to 4h
1014 head-fixation, sleep imaging sessions were recorded, which were synchronized with
1015 recordings of the pupil and running speed. Sleep imaging was performed during the light phase
1016 of the dark/light cycle.

1017 *Two-photon spine imaging in anesthetized and awake mice*

1018 3 - 4 weeks after window implantation, chronic spine imaging started in Tg(Thy1-EGFP)MJrs/J
1019 mice with the first of a total of four imaging series (see Fig. S10A). Each imaging series was
1020 done under one of the three anesthetic conditions (Iso, Keta/Xyl, MMF, see above for details)
1021 or during wakefulness. Within one series, mice were imaged 5 times every 4 days. Afterwards,
1022 mice were allowed to recover for three to four weeks until the next imaging series under a
1023 different anesthetic condition was started. Thus, each experiment lasted approx. 5 months. To
1024 avoid time-dependent effects, anesthetic conditions were pseudo-randomized (see Fig. S10A).
1025 For imaging sessions under anesthesia mice were head fixed under the microscope on a
1026 heated blanket to maintain body temperature. Eyes were covered with eye ointment (Vidisic,
1027 Bausch + Lomb) to prevent drying. The window was centered under the two-photon
1028 microscope (MOM-scope, Sutter Instruments, modified by Rapp Optoelectronics) and GFP
1029 expression was verified in the hippocampus using epi-fluorescence. Image acquisition was
1030 carried out with a Ti:Sa laser (Chameleon Vision-S, Coherent) tuned to 980 nm to excite GFP.
1031 Images were acquired with a 40x water immersion objective (Nikon CFI APO NIR 40X W, 0.80
1032 NA, 3.5 mm WD). Single planes (512x512 pixels) were acquired at 30 Hz with a resonant
1033 scanner at 10-60 mW (980 nm) using ScanImage 2017b. Before the first imaging session, we
1034 registered the field of views with the help of vascular landmarks and cell bodies of CA1
1035 pyramidal neurons and selected several regions for longitudinal monitoring across the duration
1036 of the time-lapse experiment. Each of these regions contained between 1 and 2 dendritic
1037 segments visibly expressing GFP. The imaging sessions lasted for max 60 min and mice were
1038 placed back to their home cages where they woke up.

1039 *Morris Water Maze*

1040 We designed a protocol for reversal learning in the spatial version of the water maze to assess
1041 the possible effects of the different anesthetics on episodic-like memory in mice [98, 99]. The
1042 water maze consisted of a circular tank (145 cm in diameter) circled by dark curtains and walls.
1043 The water was made opaque by the addition of non-toxic white paint such that the white
1044 platform (14 cm diameter, 9 cm high, 1 cm below the water surface) was not visible. Four
1045 landmarks (35 X 35 cm) differing in shape and grey gradient were positioned on the wall of the
1046 maze. Four white spotlights on the floor around the swimming pool provided homogeneous

1047 indirect illumination of 60 lux on the water surface. Mice were first familiarized for one day to
1048 swim and climb onto a platform (diameter of 10 cm) placed in a small rectangular maze (42.5
1049 x 26.5 cm and 15.5 cm high). During familiarization, the position of the platform was
1050 unpredictable since its location was randomized, and training was performed in darkness. After
1051 familiarization, mice underwent three learning days, during which they had to learn the location
1052 of a hidden platform. The starting position and the side of the maze from which mice were
1053 taken out of the maze were randomized. On day 1, mice underwent four learning trials
1054 (maximum duration of 90 seconds, inter-trial interval of 10 minutes). After staying on the
1055 platform for 15 s, mice were returned to their home cage and warmed up under red light. On
1056 day 2, mice underwent two training trials before they performed a 60 seconds-long probe trial
1057 to assess their searching strategy. Afterwards, one additional training trial was used to re-
1058 consolidate the memory of the platform position, and mice were distributed into four groups
1059 with a similar distribution of performance. On day 3, the long-term memory of the platform
1060 position was tested with a 45-seconds long probe trial, followed by another training trial with
1061 the platform in place to avoid extinction. Then mice underwent four reversal learning trials with
1062 the platform located in the quadrant opposite the one in which the platform was during the
1063 previous training trials. To assess whether the mice learned the new platform position, mice
1064 underwent a 60-seconds long probe trial followed by one more training trial to consolidate the
1065 memory of the new location. One hour after the last reversal learning trial, mice were
1066 anesthetized to analyze the effects of the anesthesia on the consolidation of the memory of
1067 the new platform position. Mice were assigned to four groups with an equal average
1068 performance during the probe trial on day 2. Each group was subjected to different conditions:
1069 one-hour Iso anesthesia, one-hour MMF anesthesia, Keta/Xyl anesthesia (which was not
1070 antagonized), and one group was left untreated. On day 4, mice underwent a 60-seconds long
1071 probe trial to evaluate their searching strategies; namely, the "episodic-like memory" of the
1072 reversal learning trials performed one hour before having been anesthetized on day 3 (see Fig.
1073 9A).

1074 **Quantification and Statistical Analysis**

1075 *Electrophysiology*

1076 In vivo electrophysiology data were analyzed with custom-written scripts in the Matlab
1077 environment available at https://github.com/mchini/HanganuOpatzToolbox. We selected the
1078 recording site in the pyramidal layer of CA1. Data were band-pass filtered (1-100 Hz or 0-
1079 100 Hz for low frequency LFP analysis) using a third-order Butterworth forward and backward
1080 filter to preserve phase information before down-sampling to analyze LFP.

1081 *Detection of active periods.* Active periods were detected with an adapted version of an
1082 algorithm   for   ripple   detection
1083 (https://github.com/buzsakilab/buzcode/blob/master/detectors/detectEvents/bz_FindRipples.
1084 m). Briefly, active periods were detected on the band-pass filtered (4-20 Hz) normalized
1085 squared signal using both absolute and relative thresholds. We first passed the signal through
1086 a boxcar filter and then performed hysteresis thresholding: we first detected events whose
1087 absolute or relative power exceeded the higher threshold, and considered as belonging to the
1088 same event all data points that were below the lower (absolute or relative) threshold. Absolute
1089 thresholds were set to 7 and 15 µV, relative thresholds to 1 and 2. Periods were merged if
1090 having an inter-period interval shorter than 900 ms, and discarded if lasted less than 500 ms.
1091 Percentage of active periods was calculated for 15 min bins. Timestamps were preserved for
1092 further analysis.

1093   *Power spectral density.* Power spectral density was calculated on 30 s-long windows of 0-100
1094   Hz filtered signal using Welch's method with a signal overlap of 15 s.

1095   *Modulation index (MI).* Modulation index was calculated as (value anesthesia - value pre-
1096   anesthetized) / (value anesthesia + value pre-anesthetized).

1097   *Power law decay exponent of the LFP power spectrum.* The 1/f slope was computed as in [36].
1098   We used robust linear regression (Matlab function *robustfit.m*) on the log10 of the LFP power
1099   spectrum in the 30-50 Hz frequency range.

1100   *Phase-amplitude coupling (PAC).* PAC was calculated on 0-100 Hz filtered full signal using the
1101   PAC toolbox based on modulation index measure [100]. Range of phase vector was set to 0-
1102   8 Hz and range of amplitude vector was set to 20-100 Hz. Significant coupling was calculated
1103   in comparison to a shuffled dataset. Non-significant values were rejected.

1104   *Single unit analysis.* Single unit activity (SUA) was detected and clustered using klusta [101]
1105   and manually curated using phy (https://github.com/cortex-lab).

1106   *Active units:* the recording was divided into 15-minute bins. Single units were considered to be
1107   active in the time interval if they fired at least five times.

1108   *Pairwise phase consistency.* Pairwise phase consistency (PPC) was computed as previously
1109   described [102]. Briefly, the phase in the band of interest was extracted as mentioned above,
1110   and the mean of the cosine of the absolute angular distance (dot product) among all single unit
1111   pairs of phases was calculated.

1112   *Unit Power.* SUA spike trains of each recording were summed in a population vector, and
1113   power spectral density was calculated on 30 s-long windows using Welch's method with a
1114   signal overlap of 15 s. The resulting power spectra were normalized by the firing rate in that
1115   window.

1116   *Spike-Time tiling coefficient* (STTC) was computed as previously described [52]. Briefly, we
1117   quantified the proportion (P_A) of spikes of spike train A that fall within ±Δt of a spike from spike
1118   train B. To this value we subtract the proportion of time that occurs within ±Δt of spikes from
1119   spike train B (T_B). This is then divided by 1 minus the product of these two values. The same
1120   is then applied after inverting spike train A and B, and the mean between the two values is
1121   kept.

1122

$$STTC = \frac{1}{2}\left(\frac{P_A - T_B}{1 - P_A T_B} + \frac{P_B - T_A}{1 - P_B T_A}\right)$$

1123   Importantly, this coefficient has several desirable properties. It is bounded between -1 and 1.
1124   It is symmetric with respect to the two spike trains. Computing it over different timescales is
1125   readily done by controlling the value of the parameter "Δt". Lastly, and most importantly,
1126   traditionally used methods of assessing correlations between pairs of spike trains show an
1127   inverse correlation between their value and firing rate, due to the fact that spiking is sparse
1128   with respect to the sampling frequency, and therefore quiescent period in both spike trains
1129   artificially increase the correlation. This is not the case for the spike-time tiling coefficient [52].
1130   Given that there are large differences in the average firing rate of our conditions, we chose
1131   STTC analysis over pure correlation analysis to circumvent this major bias. On the flipside,
1132   STTC cannot be straightforwardly applied to negative correlations, that were therefore not
1133   investigated in SUA data.

1134   *Calcium imaging data*

1135 In vivo calcium imaging data were analyzed with custom-written scripts in the Python and
1136 Matlab environment available at https://github.com/mchini/Yang_Chini_et_al.

1137 *Alignment of multiple recordings.* To track the activity of the same set of neurons in different
1138 anesthetic conditions and during wakefulness, we acquired two-photon time series of a defined
1139 field of view for each animal and each condition across multiple weeks. Over such long time
1140 periods, the field of view was susceptible to geometrical transformations from one recording to
1141 another and thus, any two time series were never perfectly aligned. This problem scaled with
1142 time that passed between recordings. However, optimal image alignment is critical for the
1143 successful identification and calcium analysis of the same neurons across time [103, 104].

1144 To address this problem, we developed an approach based on the pystackreg package, a
1145 Python implementation of the ImageJ extension TurboReg/StackReg [105]. The source code
1146 that reproduces the procedure described in this section is available on github
1147 (https://pypi.org/project/pystackreg/). The *pystackreg* package is capable of using different
1148 combinations of geometrical transformations for the alignment. We considered rigid body
1149 (translation + rotation + scaling) and affine (translation + rotation + scaling + shearing)
1150 transformation methods, which we applied to mean and enhanced-mean intensity images
1151 generated by Suite2p during the registration of each single recording. We performed the
1152 alignment using all four combinations (2 transformations x 2 types of images) choosing the one
1153 with the best performance according to the following procedure. Squared difference between
1154 the central part of a reference and aligned image served as a distance function d to quantify
1155 the alignment (since the signal is not always present on the borders of the image they were
1156 truncated):

1157
$$d = \sum_{i,j}^{\substack{Tranc.\\images}} (x_{i,j}^{ref} - x_{i,j}^{aligned})^2,$$

1158 where $x_{i,j}^{ref}$ and $x_{i,j}^{aligned}$ are intensities of the pixel with coordinates i,j of the reference and
1159 aligned images. The combination with the smallest score was chosen for the final
1160 transformation. In some rare cases, the algorithm of the alignment did not converge for a given
1161 transformation method and image type (mean or enhanced-mean), crumbling the aligned
1162 image in a way that most of the field of view remained empty. This combination may have the
1163 smallest distance function *d* and may be falsely identified as the best one. To overcome this
1164 issue, an additional criterion was applied, which requires the central part of the aligned picture
1165 to contain more than 90 % of the non-empty pixels. The overall performance of the algorithm
1166 was verified by visual inspection. An example of the alignment of two recordings is shown in
1167 Fig. S5. The alignment for all recordings of an example mouse is demonstrated in a
1168 supplementary video (Supplementary_video_37529_aligned_recordings.avi).

1169 In case of relatively small distortions across recordings, for example, when consecutive
1170 acquisitions were done within one imaging session, registration can alternatively be performed
1171 simultaneously with ROI detection in Suite2p by concatenating those TIFF-stacks. In this
1172 approach, every ROI is automatically labeled with the same identification number across all
1173 recordings.

1174 *Identification of the same neurons across different recordings & unique neuron ID assignment.*
1175 After the alignment procedure, we set out to identify neurons which were active across multiple
1176 recordings (and thus, multiple conditions). To achieve this, we developed an algorithm similar
1177 to the one described in Sheintuch. et al. 2017 [104]

34

1178 The algorithm processes in series all recordings for a given animal and assigns unique
1179 identification (ID) numbers to each ROIs of every recording. Since the recordings under Iso-
1180 anesthesia had the largest number of active neurons, we chose the first recording of this
1181 condition as reference. We assigned IDs that ranged from 1 to the total amount of neurons to
1182 all the ROIs of this recording. For every other recording of each mouse, Neuron ID assignment
1183 consisted of: 1. comparison of the properties (details below) of each ROI with each ROI that
1184 had already been processed. 2a. If the properties of the ROI matched the properties of an ROI
1185 from a previously analyzed recording, the ROI received the same Neuron ID. 2b. If no match
1186 was found, a new (in sequential order) Neuron ID was assigned to the ROI. In order to be
1187 identified as representing the same neuron in two different recordings, two ROIs had to respect
1188 the following criteria: the distance between their centroids had to be below 3 µm, and the
1189 overlap between their pixels had to be above 70%. An example of the identification of unique
1190 neuron pairs in two recordings is presented in Fig. S6A. The thresholds were chosen based
1191 on the distribution of the distances between centroids and percentage of the overlaps. An
1192 example for a single mouse is graphically illustrated in Fig. S6B. Both properties have a clearly
1193 bimodal distribution (similar to [104]) with cutoffs close to the chosen thresholds.

1194 *Signal extraction and analysis.* Signal extraction, correlation and spectral analysis for calcium
1195 signal was performed using Python (Python Software Foundation, NH, USA) in the Spyder
1196 (Pierre Raybaut, The Spyder Development Team) development environment. Calcium imaging
1197 data were analyzed with the Suite2p toolbox [106] using the parameters given in table 1.

1198

Parameter	Variable	Value
Sampling rate, frames per second	fs	30
Registration		
Subsampled frames for finding reference image	nimg_init	2000
Number of frames per batch	batch_size	200
Maximum allowed registration shift, as a fraction of frame max(width and height)	maxregshift	0.1
Precision of subpixel registration (1/subpixel steps)	subpixel	10
Smoothing	smooth_sigma	1.15
Bad frames to be excluded	th_badframes	100.0
Non-rigid registration		
Use nonrigid registration	nonrigid	True
Block size to register (** keep this a multiple of 2 **)	block_size	[128,128]
if any nonrigid block is below this threshold, it gets smoothed until above this threshold. 1.0 results in no smoothing	snr_thresh	2.0
maximum pixel shift allowed for nonrigid, relative to rigid	maxregshiftNR	10

Cell detection		
Run ROI extraction	roidetect	True
Run sparse_mode	sparse_mode	False
Diameter for filtering and extracting	diameter	12.0
Keep ROIs fully connected (set to 0 for dendrites)	connected	True
Maximum number of binned frames for cell detection	nbinned	5000
Maximum number of iterations to do cell detection	max_iterations	20
Adjust the automatically determined threshold by this scalar multiplier	threshold_scaling	1.0 or 0.1
Cells with more overlap than this get removed during triage, before refinement	max_overlap	0.75
Running mean subtraction with window of size 'high_pass'	high_pass	100
ROI extraction		
Number of pixels to keep between ROI and neuropil donut	inner_neuropil_radius	2
Minimum number of pixels in the neuropil	min_neuropil_pixels	100
Pixels that are overlapping are thrown out (False) or added to both ROIs (True)	allow_overlap	True
Deconvolution		
Deconvolution time constant, seconds	tau	0.7

1199

1200 The same analytical pipeline was applied to both the raw fluorescence traces as well as the
1201 deconvolved ("spikes") signal, as extracted by the Suite2p toolbox. Generally, the raw
1202 fluorescence signal was preferred over the deconvolved one given that its extraction is more
1203 straightforward and relies on less assumptions. However, while the reported effects varied in
1204 magnitude depending on which of the two signals was considered, the same results were
1205 obtained on both datasets. The effects were entirely consistent. For raw signal analysis of each
1206 neuron, previous to any further step, we subtracted 0.7 of the corresponding neuropil
1207 fluorescence trace.

1208 The number and height of calcium transients properties were calculated with the scipy function
1209 *find_peaks* on the raw calcium traces with the following parameters: height = 200, distance =
1210 10 and prominence = 200. The decay was computed on the 10 best-isolated transients of each
1211 neuron, using the *OASIS* toolbox (https://github.com/j-friedrich/OASIS). We used the
1212 *deconvolve* function with the following parameters: penalty = 0, optimize_g = 10. Traces with
1213 an estimated decay over 2 seconds were considered cases of failed extraction and removed
1214 from further analysis.

1215 The choice of the parameter values for transient detection is somewhat arbitrary. Similarly, it
1216 is debatable whether and how the calcium traces should best be normalized. Therefore, we
1217 tested the robustness of our findings by systematically varying signal extraction choices. We
1218 first varied the height and prominence threshold across a wide range of values (50 to 700
1219 arbitrary units). We further computed transients features on normalized ΔF/F calcium traces.
1220 To normalize calcium signals, we used the baseline value as extracted by the *deconvolve*
1221 function. Also, in this case, we varied the height and prominence threshold across a wide range
1222 of values (0.5 to 3 arbitrary units). Finally, we computed two measures of neuronal activity that
1223 are independent of calcium transients detection: the average of the trace integral and its
1224 standard deviation, with and without normalization. Across all of these scenarios, the reported
1225 effects were robustly consistent.

1226 Correlations were computed both as Pearson (numpy function *corrcoeff*) and Spearman
1227 (custom written function) coefficient on the z-scored signal. To both sets of coefficients, the
1228 Fisher correction (the inverse of the hyperbolic tangent function, numpy function *arctanh*) was
1229 applied. For power analysis, we first created a population activity vector by summing all the
1230 single neuron z-scored signals, and then estimated the power spectral density by applying the
1231 Welch method (sampling frequency = 30 Hz, number of points for fast Fourier transformation
1232 = 1024, no overlap, window length = 1 s).

1233 For analysis of recovery from anesthesia, all recordings of the imaging session for a given
1234 animal were concatenated in Suite2p. As a consequence, each recording in the imaging
1235 session has the same set of reconstructed neurons. A time window of 5000 frames was used
1236 for the analysis to ensure continuous motionless periods. To track the neuronal activity
1237 changes, the number of fluorescence peaks, their amplitude, and the characteristic decay
1238 constant of the transients were considered. Each imaging session's threshold was chosen to
1239 match the median activity in the pre-anesthesia (awake) state across all animals. To assess
1240 the relative changes of these parameters induced by anesthesia and their subsequent
1241 recovery over time, the parameters were normalized to their median value at the pre-
1242 anesthesia (awake) state. Notably, we focused our analysis on neurons that maintained some
1243 detectable activity during anesthesia, and neurons with no detected peaks were excluded from
1244 the distributions. Additionally, we applied the cut *decay constant* > 1/30 [s] (where 30 frames
1245 per second is an acquisition rate) to remove the traces where the OASIS algorithm considered
1246 a single noise peak to be a calcium transient.

1247 Complexity analysis was performed in the Matlab (MathWorks) environment. For complexity
1248 analysis, we limited the number of neurons to the minimum (N_{min}) present in any recording of
1249 any condition for each single mouse (median = 265, min = 156, max = 1068). The resulting
1250 matrix therefore had the $T_{rec}xN_{min}$ dimensions, where T_{rec} represents the time vector for the
1251 recording, with a length of 5 min and a sampling rate of 30 Hz. For recordings that had a
1252 number of neurons larger than N_{min} for that mouse, we randomly sampled n = N_{min} neurons
1253 and repeated the analysis 5 times. For every extracted parameter, we then considered the
1254 median value over the 5 repetitions. For further analysis, the signal was down sampled from
1255 the original sampling frequency of 30 Hz to 10 Hz (100 ms bins). The same analytical pipeline
1256 was then applied to both the raw fluorescence traces, as well as the deconvolved signal.

1257 *tSNE clustering.* tSNE clustering was performed similar to [26]. Briefly, in a range between 5
1258 and 45, the perplexity value that minimized the reconstruction error was selected. The number
1259 of PCA components used for this step was limited to 30. For the raw fluorescence signal,
1260 Euclidian distance was used, whereas for the deconvolved signal we opted for cosine distance,
1261 as it is better suited to a sparse signal. We computed the probability distribution of the resulting

37

1262 embedded matrix ($2xT_{rec}$), that was then convolved with a 2D Gaussian window (standard
1263 deviation was set to be equal to 1/40 of the total maximum value). To evaluate the number of
1264 clusters in the distribution, we then applied a series of standard steps in image analysis:
1265 background subtraction with the rolling ball method, smoothing with a median filter,
1266 thresholding, watershedding to avoid undersegmentation, and extended minima
1267 transformation. Finally, the exterior boundaries of the objects were traced and counted. This
1268 gave the number of clusters.

1269 *Affinity Propagation Clustering (APC).* Affinity Propagation clustering was performed using a
1270 Matlab toolbox [https://www.psi.toronto.edu/index.php?q=affinity%20propagation] and
1271 similarly to [26]. We first obtained a distance map, which was computed as 1 minus the
1272 pairwise cosine distance between observations of the $T_{rec}xN_{min}$ matrix. This distance matrix
1273 was then fed to the affinity propagation algorithm with the input preference set equal to the
1274 median of the distance matrix.

1275 *Principal Component Analysis (PCA) clustering and variance explained.* Standard PCA was
1276 applied to the $T_{rec}xN_{min}$ matrix. The number of clusters was computed as the number of
1277 components that was needed to cumulatively explain 90% of the variance of the input matrix.
1278 Further, we computed the loglog decay coefficient of number of components versus variance
1279 explained.

1280 *Community detection.* To detect communities, we used the Louvain algorithm from the Brain
1281 Connectivity Toolbox (https://sites.google.com/site/bctnet/), a modularity maximization
1282 procedure widely used in studies examining brain networks [107]. This approach aims at
1283 subdividing the network into partitions that are more internally dense than would be expected
1284 by chance [53]. As input to the algorithm, we used Fisher-transformed correlation matrices
1285 obtained from calcium imaging time-series. Matrices were not thresholded, and both positive
1286 and negative correlations were taken into account to determine optimal modular partitions. The
1287 algorithm was evaluated while varying the resolution parameter gamma between 0 and 3, in
1288 steps of 0.1. For the multiresolution approach and hierarchical consensus clustering, data was
1289 analyzed using code available at https://github.com/LJeub/HierarchicalConsensus and
1290 according to the procedure described in [55]. The number of communities detected by the
1291 finest level partition of the consensus hierarchy was used for further analysis. While neurons
1292 in the awake condition tended to be spatially closer to each other than for the other conditions
1293 (Fig. S8E), this is unlikely to have influenced the results of the analysis, as the difference was
1294 minimal and there was no correlation between median distance in a recording and the number
1295 of detected communities (Fig. S8F).

1296 *Sleep scoring*

1297 Sleep scoring was carried out in two steps. We first used electrophysiological features (see
1298 below) to classify the behavioral state of the electrophysiological recordings. Then, using this
1299 dataset as ground truth, we extracted pupil/eyelid features that we used to extend our
1300 classification to the calcium imaging recordings.

1301 *Electrophysiological recordings.* We divided the signal in 30s epochs with a 50% overlap, and
1302 used a rule-based approach similar to that applied in [57, 108]. NREM sleep epochs were
1303 defined as epochs having LFP power in the delta band (1-4 Hz) higher than the 70th percentile,
1304 EMG broadband (30-300 Hz) power lower than the median, and no movement. REM sleep
1305 epochs were defined as epochs having a ratio between theta (6-12 Hz) and delta LFP power
1306 higher than the 70th percentile, EMG broadband power lower than the 25th percentile, and no
1307 movement. Finally, wakefulness epochs were defined as epochs having EMG broadband

1308   power that exceeded the 80th percentile or with mouse movement. Given that this rule-based
1309   approach left ~49% of the epochs as unclassified, we extended this classification with a
1310   machine-learning approach using the scikit-learn toolbox [109]. Using the classified epochs as
1311   the labelled dataset, we trained a K-nearest neighbors classifier (*number of neighbors=20,*
1312   *weights=distance, algorithm=auto, leaf size=5, p=2, scoring=f1 macro*) to which we fed the
1313   following quantile-transformed (*quantiles=20*) features: LFP power in the delta and theta band,
1314   ratio between LFP delta and theta power, EMG broadband power and average movement.
1315   After training, the algorithm was asked to predict the unclassified epochs. Predictions that were
1316   done with a probability estimate above 99% were kept, the others were left as unclassified.
1317   This adjunction to the rule-based approach allowed us to lower the percentage of unclassified
1318   (uncertain) epochs to ~28%.

1319   *Pupil and eyelid analysis.* During electrophysiological recordings, the eye of the mouse was
1320   recorded with a monochrome, infrared sensitive camera (UI-3360CP-NIR-GL Rev. 2, iDS
1321   imaging, Germany, objective: LMZ45T3 2/3" 18-108mm/F2.5 manual macro zoom lens, Kowa,
1322   Germany) under red light. Videos were captured with the uEye Cockpit software (iDS imaging,
1323   Germany) with a framerate of 30 Hz. Pupil, EMG and electrophysiological recordings were
1324   synchronized with a customized light/digital pulse shutter. During calcium imaging recordings
1325   were done with a , infrared sensitive camera (DMK 33UX249; The Imaging Source, Germany)
1326   equipped with a macro objective (TMN 1.0/50; The Imaging Source, Germany) at a frame rate
1327   of 10 Hz. Contours of the mouse eye were tracked using the deep neural network-based
1328   software module DeepLabCut [110] and subsequently processed in MATLAB. We trained a
1329   neural network (residual neural network, 152 layers, 200,000 iterations) to detect the upper,
1330   lower, left, and right edges of the pupil and eyelid, respectively, in images down-sampled to
1331   256 pixels on the shorter edge (n = 1038 frames for videos from electrophysiology, n = 2255
1332   frames for videos from calcium imaging). Besides the position of each tracked point,
1333   DeepLabCut provides a value quantifying the certainty about the determined position (which
1334   is low in the case of occluded objects, e.g. the pupil during an eyeblink). Samples with a
1335   certainty < 0.5 were linearly interpolated from the last point before to the first point after the
1336   respective samples which had a certainty of > 0.5 (0.24/0.56 % of total pupil samples and
1337   0.11/0.12 % of total eyelid samples acquired during electrophysiology and calcium imaging
1338   experiments, respectively). We then calculated the pupil diameter (as the maximum distance
1339   between two opposing points of the pupil) as well as its center of mass, and the opening of the
1340   eye (as the distance between the top and the bottom eyelid). Finally, blinks were removed from
1341   the eye-opening data by linearly interpolating regions which exceed the moving median minus
1342   three times moving median absolute deviation (sliding window = 30 s).

1343   *Calcium imaging recordings.* Using the expanded classification of the electrophysiology
1344   dataset, we extracted the following pupil/eyelid features: maximum and minimum pupil
1345   diameter, standard deviation of the pupil diameter, pupil area, pupil motion and eyelid distance.
1346   We then tested the extent to which it was possible to correctly predict the behavioral state on
1347   these features alone, similarly to Yüzgec et al., 2018. To this aim, we quantile transformed
1348   these features (*quantiles=[50, 100, 500]*), and passed them to a K-nearest neighbors classifier
1349   with similar hyper-parameters as the previous one (*number of neighbors=[5, 10],*
1350   *weights=uniform, algorithm=auto, leaf size=1, p=2, scoring=f1 macro).* Hyper-parameter
1351   tuning was done using GridSearchCV. We then iteratively (n=100) tested the prediction
1352   accuracy on 25% of the dataset, yielding good average accuracy for wakefulness (~86%) and
1353   NREM sleep (~90%). On the contrary, most REM sleep was classified as NREM (~62%) and
1354   the accuracy for this category was significantly lower (~27%). Finally, we retrained the classifier

1355   on the entire dataset of pupil/eyelid electrophysiological features, and used it to predict the
1356   behavioral state of the calcium imaging dataset.

1357

1358   *Two-Photon Spine Image Processing*

1359   In each animal, at least one GFP-expressing CA1 pyramidal neuron was selected and 1-3
1360   dendrites of 20–50 μm length of each of the following types were analyzed: basal dendrites,
1361   oblique dendrites emerging from the apical trunk and tuft dendrites. Motion artefacts were
1362   corrected with a custom-modified Lucas-Kanade-based alignment algorithm written in Matlab.
1363   Spines that laterally emanated from the dendrite were counted by manually scrolling through
1364   the z-stacks of subsequent imaging time points of the same dendritic element, by an expert
1365   examiner blinded to the experimental condition. Protrusions from the dendrite that reached a
1366   threshold of 0.2 μm were scored as dendritic spines regardless of shape. If spine neck
1367   positions differed 0.5 μm on the subsequent images, the spine was scored as a new spine.
1368   Spines were scored as lost if they fell below the threshold of 0.2 μm. Spine density was
1369   calculated as the number of spines per μm. The turnover ratio was calculated for every time
1370   point by dividing the sum of gained and lost spines by the number of present spines. The
1371   survival fraction of spines was calculated as the percentage of remaining spines compared
1372   with the first imaging time point.

1373   *Statistical analysis*

1374   Statistical analyses were performed using R Statistical Software (Foundation for Statistical
1375   Computing, Vienna, Austria) or GraphPad Prism. All R scripts and datasets are available on
1376   GitHub https://github.com/mchini/Calcium-Imaging---Anesthesia. Nested data were analyzed
1377   with linear mixed-effect models to account for the commonly ignored increased false positive
1378   rate inherent in nested design [111]. We used "mouse", "recording", "neuron" (calcium
1379   imaging), and "single unit" (electrophysiology) as random effects, according to the specific
1380   experimental design. Parameter estimation was done using the lmer function implemented in
1381   the *lme4* R package [112]. Model selection was performed according to experimental design.
1382   Significance and summary tables for lmer model fits were evaluated with the *lmerTest* R
1383   package [113], using the Satterthwaite's degrees of freedom method. Post hoc analysis with
1384   Tukey multiple comparison correction was carried out using the *emmeans* R package.

1385

1386   **Data Availability**

1387   Further information and requests for resources and reagents should be directed to and will
1388   be fulfilled by the corresponding author, J. Simon Wiegert (simon.wiegert@zmnh.uni-
1389   hamburg.de).

1390   *Data and Code Availability*

1391   The code generated during this study is available at
1392   https://github.com/OpatzLab/HanganuOpatzToolbox and https://github.com/mchini/Calcium-
1393   Imaging---Anesthesia

1394   The calcium imaging and electrophysiology data sets generated during this study are
1395   available at https://gin.g-node.org/SW_lab/Anesthesia_CA1

1396

REFERENCES

1.   Rudolph U, Antkowiak B. Molecular and neuronal substrates for general anaesthetics. Nat Rev Neurosci. 2004;5(9):709-20. Epub 2004/08/24. doi: 10.1038/nrn1496. PubMed PMID: 15322529.

2.   Urban BW, Bleckwenn M. Concepts and correlations relevant to general anaesthesia. Br J Anaesth. 2002;89(1):3-16. Epub 2002/08/14. doi: 10.1093/bja/aef164. PubMed PMID: 12173238.

3.   Sanders RD, Tononi G, Laureys S, Sleigh JW. Unresponsiveness not equal unconsciousness. Anesthesiology. 2012;116(4):946-59. Epub 2012/02/09. doi: 10.1097/ALN.0b013e318249d0a7. PubMed PMID: 22314293; PubMed Central PMCID: PMCPMC3311716.

4.   Alkire MT, Hudetz AG, Tononi G. Consciousness and anesthesia. Science. 2008;322(5903):876-80. Epub 2008/11/08. doi: 10.1126/science.1149213. PubMed PMID: 18988836; PubMed Central PMCID: PMCPMC2743249.

5.   Mashour GA, Orser BA, Avidan MS. Intraoperative awareness: from neurobiology to clinical practice. Anesthesiology. 2011;114(5):1218-33. Epub 2011/04/06. doi: 10.1097/ALN.0b013e31820fc9b6. PubMed PMID: 21464699.

6.   Antognini JF, Carstens E. In vivo characterization of clinical anaesthesia and its components. Br J Anaesth. 2002;89(1):156-66. Epub 2002/08/14. doi: 10.1093/bja/aef156. PubMed PMID: 12173227.

7.   Vutskits L, Xie Z. Lasting impact of general anaesthesia on the brain: mechanisms and relevance. Nat Rev Neurosci. 2016;17(11):705-17. Epub 2016/10/19. doi: 10.1038/nrn.2016.128. PubMed PMID: 27752068.

8.   Zurek AA, Yu J, Wang DS, Haffey SC, Bridgwater EM, Penna A, et al. Sustained increase in alpha5GABAA receptor function impairs memory after anesthesia. J Clin Invest. 2014;124(12):5437-41. Epub 2014/11/05. doi: 10.1172/JCI76669. PubMed PMID: 25365226; PubMed Central PMCID: PMCPMC4348961.

9.   Neves G, Cooke SF, Bliss TV. Synaptic plasticity, memory and the hippocampus: a neural network approach to causality. Nat Rev Neurosci. 2008;9(1):65-75. Epub 2007/12/21. doi: 10.1038/nrn2303. PubMed PMID: 18094707.

10.   Larkum M. A cellular mechanism for cortical associations: an organizing principle for the cerebral cortex. Trends Neurosci. 2012. Epub 2013/01/01. doi: 10.1016/j.tins.2012.11.006. PubMed PMID: 23273272.

11.   Segal M. Dendritic spines and long-term plasticity. Nat Rev Neurosci. 2005;6(4):277-84. Epub 2005/04/02. doi: 10.1038/nrn1649. PubMed PMID: 15803159.

12.   Kasai H, Fukuda M, Watanabe S, Hayashi-Takagi A, Noguchi J. Structural dynamics of dendritic spines in memory and cognition. Trends Neurosci. 2010;33(3):121-9. Epub 2010/02/09. doi: S0166-2236(10)00002-0 [pii]

10.1016/j.tins.2010.01.001. PubMed PMID: 20138375.

13.   Frey U, Morris RG. Synaptic tagging and long-term potentiation. Nature. 1997;385(6616):533-6. PubMed PMID: 9020359.

14.   Yang G, Pan F, Gan WB. Stably maintained dendritic spines are associated with lifelong memories. Nature. 2009;462(7275):920-4. Epub 2009/12/01. doi: 10.1038/nature08577. PubMed PMID: 19946265.

1443   15.   Wiegert JS, Pulin M, Gee CE, Oertner TG. The fate of hippocampal synapses depends
1444   on the sequence of plasticity-inducing events. eLife. 2018;7. Epub 2018/10/13. doi:
1445   10.7554/eLife.39151. PubMed PMID: 30311904; PubMed Central PMCID: PMCPMC6205809.

1446   16.   Wiegert JS, Oertner TG. Long-term depression triggers the selective elimination of
1447   weakly integrated synapses. Proc Natl Acad Sci U S A. 2013;110(47):E4510-9. Epub
1448   2013/11/06. doi: 10.1073/pnas.1315926110. PubMed PMID: 24191047; PubMed Central
1449   PMCID: PMCPMC3839749.

1450   17.   De Roo M, Klauser P, Muller D. LTP promotes a selective long-term stabilization and
1451   clustering of dendritic spines. PLoS Biol. 2008;6(9):e219. Epub 2008/09/16. doi:
1452   10.1371/journal.pbio.0060219. PubMed PMID: 18788894; PubMed Central PMCID:
1453   PMC2531136.

1454   18.   Nagerl UV, Eberhorn N, Cambridge SB, Bonhoeffer T. Bidirectional activity-dependent
1455   morphological plasticity in hippocampal neurons. Neuron. 2004;44(5):759-67. Epub
1456   2004/12/02. doi: 10.1016/j.neuron.2004.11.016. PubMed PMID: 15572108.

1457   19.   Whitlock JR, Heynen AJ, Shuler MG, Bear MF. Learning induces long-term potentiation
1458   in the hippocampus. Science. 2006;313(5790):1093-7. PubMed PMID: 16931756.

1459   20.   Schmid LC, Mittag M, Poll S, Steffen J, Wagner J, Geis HR, et al. Dysfunction of
1460   Somatostatin-Positive Interneurons Associated with Memory Deficits in an Alzheimer's
1461   Disease Model. Neuron. 2016;92(1):114-25. doi: 10.1016/j.neuron.2016.08.034. PubMed
1462   PMID: 27641495.

1463   21.   Attardo A, Fitzgerald JE, Schnitzer MJ. Impermanence of dendritic spines in live adult
1464   CA1   hippocampus.   Nature.   2015;523(7562):592-6.   Epub   2015/06/23.   doi:
1465   10.1038/nature14467.   PubMed   PMID: 26098371;   PubMed   Central   PMCID:
1466   PMCPMC4648621.

1467   22.   Sur C, Fresu L, Howell O, McKernan RM, Atack JR. Autoradiographic localization of
1468   alpha5 subunit-containing GABAA receptors in rat brain. Brain Res. 1999;822(1-2):265-70.
1469   Epub 1999/03/20. doi: 10.1016/s0006-8993(99)01152-x. PubMed PMID: 10082908.

1470   23.   Bonin RP, Orser BA. GABA(A) receptor subtypes underlying general anesthesia.
1471   Pharmacol   Biochem   Behav.   2008;90(1):105-12.   Epub   2008/01/19.   doi:
1472   10.1016/j.pbb.2007.12.011. PubMed PMID: 18201756.

1473   24.   Chrobak JJ, Hinman JR, Sabolek HR. Revealing past memories: proactive interference
1474   and ketamine-induced memory deficits. J Neurosci. 2008;28(17):4512-20. Epub 2008/04/25.
1475   doi: 10.1523/JNEUROSCI.0742-07.2008. PubMed PMID: 18434529; PubMed Central PMCID:
1476   PMCPMC6670951.

1477   25.   Goltstein PM, Montijn JS, Pennartz CM. Effects of isoflurane anesthesia on ensemble
1478   patterns of Ca2+ activity in mouse v1: reduced direction selectivity independent of increased
1479   correlations in cellular activity. PloS one. 2015;10(2):e0118277. Epub 2015/02/24. doi:
1480   10.1371/journal.pone.0118277. PubMed PMID: 25706867; PubMed Central PMCID:
1481   PMCPMC4338011.

1482   26.   Wenzel M, Han S, Smith EH, Hoel E, Greger B, House PA, et al. Reduced Repertoire
1483   of Cortical Microstates and Neuronal Ensembles in Medically Induced Loss of Consciousness.
1484   Cell Syst. 2019;8(5):467-74 e4. Epub 2019/05/06. doi: 10.1016/j.cels.2019.03.007. PubMed
1485   PMID: 31054810; PubMed Central PMCID: PMCPMC6544156.

1486   27.   Greenberg DS, Houweling AR, Kerr JN. Population imaging of ongoing neuronal
1487   activity in the visual cortex of awake rats. Nat Neurosci. 2008;11(7):749-51. Epub 2008/06/17.
1488   doi: 10.1038/nn.2140. PubMed PMID: 18552841.

1489   28.   Soltesz I, Deschenes M. Low- and high-frequency membrane potential oscillations
1490   during theta activity in CA1 and CA3 pyramidal neurons of the rat hippocampus under

ketamine-xylazine anesthesia. J Neurophysiol. 1993;70(1):97-116. Epub 1993/07/01. doi: 10.1152/jn.1993.70.1.97. PubMed PMID: 8395591.

29.   Purdon PL, Sampson A, Pavone KJ, Brown EN. Clinical Electroencephalography for Anesthesiologists: Part I: Background and Basic Signatures. Anesthesiology. 2015;123(4):937-60. Epub 2015/08/15. doi: 10.1097/ALN.0000000000000841. PubMed PMID: 26275092; PubMed Central PMCID: PMCPMC4573341.

30.   Steriade M, Nunez A, Amzica F. A novel slow (< 1 Hz) oscillation of neocortical neurons in vivo: depolarizing and hyperpolarizing components. J Neurosci. 1993;13(8):3252-65. Epub 1993/08/01. PubMed PMID: 8340806; PubMed Central PMCID: PMCPMC6576541.

31.   Collins DR, Pelletier JG, Pare D. Slow and fast (gamma) neuronal oscillations in the perirhinal cortex and lateral amygdala. J Neurophysiol. 2001;85(4):1661-72. Epub 2001/04/05. doi: 10.1152/jn.2001.85.4.1661. PubMed PMID: 11287489.

32.   Contreras D, Steriade M. Cellular basis of EEG slow rhythms: a study of dynamic corticothalamic relationships. J Neurosci. 1995;15(1 Pt 2):604-22. Epub 1995/01/01. PubMed PMID: 7823167; PubMed Central PMCID: PMCPMC6578315.

33.   Donoghue T, Haller M, Peterson EJ, Varma P, Sebastian P, Gao R, et al. Parameterizing neural power spectra into periodic and aperiodic components. Nat Neurosci. 2020;23(12):1655-65. doi: 10.1038/s41593-020-00744-x.

34.   Trakoshis S, Martínez-Cañada P, Rocchi F, Canella C, You W, Chakrabarti B, et al. Intrinsic excitation-inhibition imbalance affects medial prefrontal cortex differently in autistic men versus women. eLife. 2020;9. doi: 10.7554/elife.55684.

35.   Lombardi F, Herrmann HJ, De Arcangelis L. Balance of excitation and inhibition determines 1/f power spectrum in neuronal networks. Chaos: An Interdisciplinary Journal of Nonlinear Science. 2017;27(4):047402. doi: 10.1063/1.4979043.

36.   Gao R, Peterson EJ, Voytek B. Inferring synaptic excitation/inhibition balance from field potentials. NeuroImage. 2017;158:70-8. Epub 2017/07/06. doi: 10.1016/j.neuroimage.2017.06.078. PubMed PMID: 28676297.

37.   Colombo MA, Napolitani M, Boly M, Gosseries O, Casarotto S, Rosanova M, et al. The spectral exponent of the resting EEG indexes the presence of consciousness during unresponsiveness induced by propofol, xenon, and ketamine. NeuroImage. 2019;189:631-44. doi: 10.1016/j.neuroimage.2019.01.024.

38.   Albrecht M, Henke J, Tacke S, Markert M, Guth B. Effects of isoflurane, ketamine-xylazine and a combination of medetomidine, midazolam and fentanyl on physiological variables continuously measured by telemetry in Wistar rats. BMC Vet Res. 2014;10:198. Epub 2014/08/26. doi: 10.1186/s12917-014-0198-3. PubMed PMID: 25149627; PubMed Central PMCID: PMCPMC4363998.

39.   Fleischmann T, Jirkof P, Henke J, Arras M, Cesarovic N. Injection anaesthesia with fentanyl-midazolam-medetomidine in adult female mice: importance of antagonization and perioperative care. Lab Anim. 2016;50(4):264-74. Epub 2016/02/11. doi: 10.1177/0023677216631458. PubMed PMID: 26860578.

40.   Canolty RT, Knight RT. The functional role of cross-frequency coupling. Trends in cognitive sciences. 2010;14(11):506-15. Epub 2010/10/12. doi: 10.1016/j.tics.2010.09.001. PubMed PMID: 20932795; PubMed Central PMCID: PMCPMC3359652.

41.   Schomburg EW, Fernandez-Ruiz A, Mizuseki K, Berenyi A, Anastassiou CA, Koch C, et al. Theta phase segregation of input-specific gamma patterns in entorhinal-hippocampal networks. Neuron. 2014;84(2):470-85. Epub 2014/09/30. doi: 10.1016/j.neuron.2014.08.051. PubMed PMID: 25263753; PubMed Central PMCID: PMCPMC4253689.

42.   Scheffer-Teixeira R, Belchior H, Caixeta FV, Souza BC, Ribeiro S, Tort AB. Theta phase modulates multiple layer-specific oscillations in the CA1 region. Cereb Cortex.

2012;22(10):2404-14. Epub 2011/11/15. doi: 10.1093/cercor/bhr319. PubMed PMID: 22079925.

43. Buzsaki G, Anastassiou CA, Koch C. The origin of extracellular fields and currents--EEG, ECoG, LFP and spikes. Nat Rev Neurosci. 2012;13(6):407-20. Epub 2012/05/19. doi: 10.1038/nrn3241. PubMed PMID: 22595786; PubMed Central PMCID: PMCPMC4907333.

44. Watson BO, Levenstein D, Greene JP, Gelinas JN, Buzsaki G. Network Homeostasis and State Dynamics of Neocortical Sleep. Neuron. 2016;90(4):839-52. Epub 2016/05/03. doi: 10.1016/j.neuron.2016.03.036. PubMed PMID: 27133462; PubMed Central PMCID: PMCPMC4873379.

45. Vinck M, Battaglia FP, Womelsdorf T, Pennartz C. Improved measures of phase-coupling between spikes and the Local Field Potential. J Comput Neurosci. 2012;33(1):53-75. Epub 2011/12/22. doi: 10.1007/s10827-011-0374-4. PubMed PMID: 22187161; PubMed Central PMCID: PMCPMC3394239.

46. Chen TW, Wardill TJ, Sun Y, Pulver SR, Renninger SL, Baohan A, et al. Ultrasensitive fluorescent proteins for imaging neuronal activity. Nature. 2013;499(7458):295-300. Epub 2013/07/23. doi: 10.1038/nature12354. PubMed PMID: 23868258; PubMed Central PMCID: PMC3777791.

47. Harris KD, Mrsic-Flogel TD. Cortical connectivity and sensory coding. Nature. 2013;503(7474):51-8. Epub 2013/11/10. doi: 10.1038/nature12654. PubMed PMID: 24201278.

48. Franks NP. General anaesthesia: from molecular targets to neuronal pathways of sleep and arousal. Nat Rev Neurosci. 2008;9(5):370-86. Epub 2008/04/22. doi: 10.1038/nrn2372. PubMed PMID: 18425091.

49. Klinzing JG, Niethard N, Born J. Mechanisms of systems memory consolidation during sleep. Nat Neurosci. 2019;22(10):1598-610. Epub 2019/08/28. doi: 10.1038/s41593-019-0467-3. PubMed PMID: 31451802.

50. Buzsaki G. Hippocampal sharp waves: their origin and significance. Brain Res. 1986;398(2):242-52. Epub 1986/11/29. doi: 10.1016/0006-8993(86)91483-6. PubMed PMID: 3026567.

51. Okun M, Steinmetz N, Cossell L, Iacaruso MF, Ko H, Bartho P, et al. Diverse coupling of neurons to populations in sensory cortex. Nature. 2015;521(7553):511-5. Epub 2015/04/08. doi: 10.1038/nature14273. PubMed PMID: 25849776; PubMed Central PMCID: PMCPMC4449271.

52. Cutts CS, Eglen SJ. Detecting pairwise correlations in spike trains: an objective comparison of methods and application to the study of retinal waves. J Neurosci. 2014;34(43):14288-303. Epub 2014/10/24. doi: 10.1523/JNEUROSCI.2767-14.2014. PubMed PMID: 25339742; PubMed Central PMCID: PMCPMC4205553.

53. Sporns O, Betzel RF. Modular Brain Networks. Annual review of psychology. 2016;67:613-40. Epub 2015/09/24. doi: 10.1146/annurev-psych-122414-033634. PubMed PMID: 26393868; PubMed Central PMCID: PMCPMC4782188.

54. Newman ME, Girvan M. Finding and evaluating community structure in networks. Phys Rev E Stat Nonlin Soft Matter Phys. 2004;69(2 Pt 2):026113. Epub 2004/03/05. doi: 10.1103/PhysRevE.69.026113. PubMed PMID: 14995526.

55. Jeub LGS, Sporns O, Fortunato S. Multiresolution Consensus Clustering in Networks. Scientific reports. 2018;8. doi: ARTN 3259

10.1038/s41598-018-21352-7. PubMed PMID: WOS:000425380900042.

56. Diekelmann S, Born J. The memory function of sleep. Nat Rev Neurosci. 2010;11(2):114-26. Epub 2010/01/05. doi: 10.1038/nrn2762. PubMed PMID: 20046194.

44

57.   Yuzgec O, Prsa M, Zimmermann R, Huber D. Pupil Size Coupling to Cortical States Protects the Stability of Deep Sleep via Parasympathetic Modulation. Curr Biol. 2018;28(3):392-400 e3. Epub 2018/01/24. doi: 10.1016/j.cub.2017.12.049. PubMed PMID: 29358069; PubMed Central PMCID: PMCPMC5807087.

58.   Chini M, Gretenkord S, Kostka JK, Popplau JA, Cornelissen L, Berde CB, et al. Neural Correlates of Anesthesia in Newborn Mice and Humans. Frontiers in neural circuits. 2019;13:38. Epub 2019/06/14. doi: 10.3389/fncir.2019.00038. PubMed PMID: 31191258; PubMed Central PMCID: PMCPMC6538977.

59.   Briner A, De Roo M, Dayer A, Muller D, Habre W, Vutskits L. Volatile anesthetics rapidly increase dendritic spine density in the rat medial prefrontal cortex during synaptogenesis. Anesthesiology.   2010;112(3):546-56.   Epub   2010/02/04.   doi: 10.1097/ALN.0b013e3181cd7942. PubMed PMID: 20124985.

60.   De Roo M, Klauser P, Briner A, Nikonenko I, Mendez P, Dayer A, et al. Anesthetics rapidly promote synaptogenesis during a critical period of brain development. PloS one. 2009;4(9):e7043. Epub 2009/09/17. doi: 10.1371/journal.pone.0007043. PubMed PMID: 19756154; PubMed Central PMCID: PMCPMC2738943.

61.   Briner A, Nikonenko I, De Roo M, Dayer A, Muller D, Vutskits L. Developmental Stage-dependent persistent impact of propofol anesthesia on dendritic spines in the rat medial prefrontal cortex. Anesthesiology. 2011;115(2):282-93. Epub 2011/06/28. doi: 10.1097/ALN.0b013e318221fbbd. PubMed PMID: 21701379.

62.   Pfeiffer T, Poll S, Bancelin S, Angibaud J, Inavalli VK, Keppler K, et al. Chronic 2P-STED imaging reveals high turnover of dendritic spines in the hippocampus in vivo. eLife. 2018;7. Epub 2018/06/23. doi: 10.7554/eLife.34700. PubMed PMID: 29932052; PubMed Central PMCID: PMCPMC6014725.

63.   Gu L, Kleiber S, Schmid L, Nebeling F, Chamoun M, Steffen J, et al. Long-term in vivo imaging of dendritic spines in the hippocampus reveals structural plasticity. J Neurosci. 2014;34(42):13948-53. Epub 2014/10/17. doi: 10.1523/JNEUROSCI.1464-14.2014. PubMed PMID: 25319691; PubMed Central PMCID: PMCPMC6705298.

64.   Portera-Cailliau C, Pan DT, Yuste R. Activity-regulated dynamic behavior of early dendritic protrusions: evidence for different types of dendritic filopodia. J Neurosci. 2003;23(18):7129-42. Epub 2003/08/09. PubMed PMID: 12904473; PubMed Central PMCID: PMCPMC6740658.

65.   Lendvai B, Stern EA, Chen B, Svoboda K. Experience-dependent plasticity of dendritic spines in the developing rat barrel cortex in vivo. Nature. 2000;404(6780):876-81. Epub 2000/04/29. doi: 10.1038/35009107. PubMed PMID: 10786794.

66.   Dailey ME, Smith SJ. The dynamics of dendritic structure in developing hippocampal slices. J Neurosci. 1996;16(9):2983-94. Epub 1996/05/01. PubMed PMID: 8622128; PubMed Central PMCID: PMCPMC6579052.

67.   Yang G, Chang PC, Bekker A, Blanck TJ, Gan WB. Transient effects of anesthetics on dendritic spines and filopodia in the living mouse cortex. Anesthesiology. 2011;115(4):718-26. Epub 2011/07/20. doi: 10.1097/ALN.0b013e318229a660. PubMed PMID: 21768874; PubMed Central PMCID: PMCPMC3815535.

68.   Moscovitch M, Cabeza R, Winocur G, Nadel L. Episodic Memory and Beyond: The Hippocampus and Neocortex in Transformation. Annual review of psychology. 2016;67:105-34. Epub 2016/01/05. doi: 10.1146/annurev-psych-113011-143733. PubMed PMID: 26726963.

69.   Nadel L, Moscovitch M. Memory consolidation, retrograde amnesia and the hippocampal complex. Curr Opin Neurobiol. 1997;7(2):217-27. Epub 1997/04/01. PubMed PMID: 9142752.

70.   O'Neill J, Pleydell-Bouverie B, Dupret D, Csicsvari J. Play it again: reactivation of waking experience and memory. Trends Neurosci. 2010;33(5):220-9. Epub 2010/03/09. doi: 10.1016/j.tins.2010.01.006. PubMed PMID: 20207025.

71.   Clark DL, Rosner BS. Neurophysiologic effects of general anesthetics. I. The electroencephalogram and sensory evoked responses in man. Anesthesiology. 1973;38(6):564-82. Epub 1973/06/01. PubMed PMID: 4145825.

72.   Sarasso S, Boly M, Napolitani M, Gosseries O, Charland-Verville V, Casarotto S, et al. Consciousness and Complexity during Unresponsiveness Induced by Propofol, Xenon, and Ketamine. Curr Biol. 2015;25(23):3099-105. Epub 2016/01/12. doi: 10.1016/j.cub.2015.10.014. PubMed PMID: 26752078.

73.   Langsjo JW, Maksimow A, Salmi E, Kaisti K, Aalto S, Oikonen V, et al. S-ketamine anesthesia increases cerebral blood flow in excess of the metabolic needs in humans. Anesthesiology. 2005;103(2):258-68. Epub 2005/07/30. doi: 10.1097/00000542-200508000-00008. PubMed PMID: 16052107.

74.   Lee U, Ku S, Noh G, Baek S, Choi B, Mashour GA. Disruption of frontal-parietal communication by ketamine, propofol, and sevoflurane. Anesthesiology. 2013;118(6):1264-75. Epub 2013/05/23. doi: 10.1097/ALN.0b013e31829103f5. PubMed PMID: 23695090; PubMed Central PMCID: PMCPMC4346246.

75.   Wei Z, Lin B-J, Chen T-W, Daie K, Svoboda K, Druckmann S. A comparison of neuronal population dynamics measured with calcium imaging and electrophysiology. PLoS computational biology. 2020;16(9):e1008198. doi: 10.1371/journal.pcbi.1008198.

76.   Katz Y, Menon V, Nicholson DA, Geinisman Y, Kath WL, Spruston N. Synapse distribution suggests a two-stage model of dendritic integration in CA1 pyramidal neurons. Neuron. 2009;63(2):171-7. Epub 2009/07/31. doi: S0896-6273(09)00510-8 [pii]

10.1016/j.neuron.2009.06.023. PubMed PMID: 19640476.

77.   Yamakage M, Hirshman CA, Croxton TL. Inhibitory effects of thiopental, ketamine, and propofol on voltage-dependent Ca2+ channels in porcine tracheal smooth muscle cells. Anesthesiology. 1995;83(6):1274-82. Epub 1995/12/01. doi: 10.1097/00000542-199512000-00018. PubMed PMID: 8533920.

78.   Yang Y, Cui Y, Sang K, Dong Y, Ni Z, Ma S, et al. Ketamine blocks bursting in the lateral habenula to rapidly relieve depression. Nature. 2018;554(7692):317-22. Epub 2018/02/16. doi: 10.1038/nature25509. PubMed PMID: 29446381.

79.   West AE, Griffith EC, Greenberg ME. Regulation of transcription factors by neuronal activity. Nat Rev Neurosci. 2002;3(12):921-31. PubMed PMID: 12461549.

80.   Wiegert JS, Bading H. Activity-dependent calcium signaling and ERK-MAP kinases in neurons: a link to structural plasticity of the nucleus and gene transcription regulation. Cell calcium. 2011;49(5):296-305. Epub 2010/12/18. doi: 10.1016/j.ceca.2010.11.009. PubMed PMID: 21163523.

81.   Hardingham GE, Bading H. Synaptic versus extrasynaptic NMDA receptor signalling: implications for neurodegenerative disorders. Nat Rev Neurosci. 2010. Epub 2010/09/16. doi: nrn2911 [pii]

10.1038/nrn2911. PubMed PMID: 20842175.

82.   Mizrahi-Kliger AD, Kaplan A, Israel Z, Bergman H. Desynchronization of slow oscillations in the basal ganglia during natural sleep. Proc Natl Acad Sci U S A. 2018;115(18):E4274-E83. Epub 2018/04/19. doi: 10.1073/pnas.1720795115. PubMed PMID: 29666271; PubMed Central PMCID: PMCPMC5939089.

1683   83.   Klausberger T, Somogyi P. Neuronal diversity and temporal dynamics: the unity of
1684   hippocampal circuit operations. Science. 2008;321(5885):53-7. Epub 2008/07/05. doi:
1685   10.1126/science.1149381. PubMed PMID: 18599766.

1686   84.   Lee D, Shtengel G, Osborne JE, Lee AK. Anesthetized- and awake-patched whole-cell
1687   recordings in freely moving rats using UV-cured collar-based electrode stabilization. Nat
1688   Protoc. 2014;9(12):2784-95. Epub 2014/11/07. doi: 10.1038/nprot.2014.190. PubMed PMID:
1689   25375992.

1690   85.   Lee AK, Manns ID, Sakmann B, Brecht M. Whole-cell recordings in freely moving rats.
1691   Neuron. 2006;51(4):399-407. Epub 2006/08/16. doi: 10.1016/j.neuron.2006.07.004. PubMed
1692   PMID: 16908406.

1693   86.   Epsztein J, Brecht M, Lee AK. Intracellular determinants of hippocampal CA1 place and
1694   silent cell activity in a novel environment. Neuron. 2011;70(1):109-20. Epub 2011/04/13. doi:
1695   10.1016/j.neuron.2011.03.006. PubMed PMID: 21482360; PubMed Central PMCID:
1696   PMCPMC3221010.

1697   87.   Pryazhnikov E, Mugantseva E, Casarotto P, Kolikova J, Fred SM, Toptunov D, et al.
1698   Longitudinal two-photon imaging in somatosensory cortex of behaving mice reveals dendritic
1699   spine formation enhancement by subchronic administration of low-dose ketamine. Scientific
1700   reports. 2018;8(1):6464. Epub 2018/04/25. doi: 10.1038/s41598-018-24933-8. PubMed PMID:
1701   29691465; PubMed Central PMCID: PMCPMC5915413.

1702   88.   Lin H, Higgins P, Loh HH, Law PY, Liao D. Bidirectional effects of fentanyl on dendritic
1703   spines and AMPA receptors depend upon the internalization of mu opioid receptors.
1704   Neuropsychopharmacology.   2009;34(9):2097-111.   Epub   2009/03/20.   doi:
1705   10.1038/npp.2009.34.   PubMed   PMID: 19295508;   PubMed   Central   PMCID:
1706   PMCPMC2731771.

1707   89.   Li N, Lee B, Liu RJ, Banasr M, Dwyer JM, Iwata M, et al. mTOR-dependent synapse
1708   formation underlies the rapid antidepressant effects of NMDA antagonists. Science.
1709   2010;329(5994):959-64. Epub 2010/08/21. doi: 10.1126/science.1190287. PubMed PMID:
1710   20724638; PubMed Central PMCID: PMC3116441.

1711   90.   Phoumthipphavong V, Barthas F, Hassett S, Kwan AC. Longitudinal Effects of
1712   Ketamine on Dendritic Architecture In Vivo in the Mouse Medial Frontal Cortex. eNeuro.
1713   2016;3(2). Epub 2016/04/12. doi: 10.1523/ENEURO.0133-15.2016. PubMed PMID:
1714   27066532; PubMed Central PMCID: PMCPMC4819286.

1715   91.   Eikermann M, Akeju O, Chamberlin NL. Sleep and Anesthesia: The Shared Circuit
1716   Hypothesis Has Been Put to Bed. Curr Biol. 2020;30(5):R219-R21. Epub 2020/03/11. doi:
1717   10.1016/j.cub.2020.01.057. PubMed PMID: 32155424.

1718   92.   Vanini G, Bassana M, Mast M, Mondino A, Cerda I, Phyle M, et al. Activation of Preoptic
1719   GABAergic or Glutamatergic Neurons Modulates Sleep-Wake Architecture, but Not Anesthetic
1720   State   Transitions.   Curr   Biol.   2020;30(5):779-87   e4.   Epub   2020/02/23.   doi:
1721   10.1016/j.cub.2019.12.063.   PubMed   PMID: 32084397;   PubMed   Central   PMCID:
1722   PMCPMC7156032.

1723   93.   Jiang-Xie LF, Yin L, Zhao S, Prevosto V, Han BX, Dzirasa K, et al. A Common
1724   Neuroendocrine   Substrate   for   Diverse   General   Anesthetics   and   Sleep.   Neuron.
1725   2019;102(5):1053-65 e4. Epub 2019/04/23. doi: 10.1016/j.neuron.2019.03.033. PubMed
1726   PMID: 31006556; PubMed Central PMCID: PMCPMC6554048.

1727   94.   Kentros C, Hargreaves E, Hawkins RD, Kandel ER, Shapiro M, Muller RV. Abolition of
1728   long-term stability of new hippocampal place cell maps by NMDA receptor blockade. Science.
1729   1998;280(5372):2121-6. Epub 1998/06/26. doi: 10.1126/science.280.5372.2121. PubMed
1730   PMID: 9641919.

1731   95.   Hayashi Y. NMDA Receptor-Dependent Dynamics of Hippocampal Place Cell
1732   Ensembles.   J   Neurosci.   2019;39(26):5173-82.   Epub   2019/04/25.   doi:

1733 10.1523/JNEUROSCI.0243-19.2019. PubMed PMID: 31015340; PubMed Central PMCID:
1734 PMCPMC6595956.

1735 96.   de Souza I, Meurer Y, Tavares PM, Pugliane KC, Lima RH, Silva RH, et al. Episodic-
1736 like memory impairment induced by sub-anaesthetic doses of ketamine. Behav Brain Res.
1737 2019;359:165-71. Epub 2018/10/26. doi: 10.1016/j.bbr.2018.10.031. PubMed PMID:
1738 30359643.

1739 97.   Zurek AA, Bridgwater EM, Orser BA. Inhibition of alpha5 gamma-Aminobutyric acid
1740 type A receptors restores recognition memory after general anesthesia. Anesth Analg.
1741 2012;114(4):845-55. Epub 2012/03/03. doi: 10.1213/ANE.0b013e31824720da. PubMed
1742 PMID: 22383672.

1743 98.   Chen G, Chen KS, Knox J, Inglis J, Bernard A, Martin SJ, et al. A learning deficit related
1744 to age and beta-amyloid plaques in a mouse model of Alzheimer's disease. Nature.
1745 2000;408(6815):975-9. Epub 2001/01/05. doi: 10.1038/35050103. PubMed PMID: 11140684.

1746 99.   Morellini F. Spatial memory tasks in rodents: what do they model? Cell Tissue Res.
1747 2013;354(1):273-86. Epub 2013/06/25. doi: 10.1007/s00441-013-1668-9. PubMed PMID:
1748 23793547.

1749 100.   Onslow AC, Bogacz R, Jones MW. Quantifying phase-amplitude coupling in neuronal
1750 network oscillations. Prog Biophys Mol Biol. 2011;105(1-2):49-57. Epub 2010/09/28. doi:
1751 10.1016/j.pbiomolbio.2010.09.007. PubMed PMID: 20869387.

1752 101.   Rossant C, Kadir SN, Goodman DFM, Schulman J, Hunter MLD, Saleem AB, et al.
1753 Spike sorting for large, dense electrode arrays. Nat Neurosci. 2016;19(4):634-41. Epub
1754 2016/03/15. doi: 10.1038/nn.4268. PubMed PMID: 26974951; PubMed Central PMCID:
1755 PMCPMC4817237.

1756 102.   Vinck M, van Wingerden M, Womelsdorf T, Fries P, Pennartz CM. The pairwise phase
1757 consistency: a bias-free measure of rhythmic neuronal synchronization. NeuroImage.
1758 2010;51(1):112-22. Epub 2010/02/02. doi: 10.1016/j.neuroimage.2010.01.073. PubMed
1759 PMID: 20114076.

1760 103.   Rose T, Jaepel J, Hubener M, Bonhoeffer T. Cell-specific restoration of stimulus
1761 preference after monocular deprivation in the visual cortex. Science. 2016;352(6291):1319-22.
1762 Epub 2016/06/11. doi: 10.1126/science.aad3358. PubMed PMID: 27284193.

1763 104.   Sheintuch L, Rubin A, Brande-Eilat N, Geva N, Sadeh N, Pinchasof O, et al. Tracking
1764 the Same Neurons across Multiple Days in Ca(2+) Imaging Data. Cell reports.
1765 2017;21(4):1102-15. doi: 10.1016/j.celrep.2017.10.013. PubMed PMID: 29069591; PubMed
1766 Central PMCID: PMCPMC5670033.

1767 105.   Thevenaz P, Ruttimann UE, Unser M. A pyramid approach to subpixel registration
1768 based on intensity. IEEE Trans Image Process. 1998;7(1):27-41. Epub 2008/02/13. doi:
1769 10.1109/83.650848. PubMed PMID: 18267377.

1770 106.   Pachitariu M, Stringer C, Dipoppa M, Schröder S, Rossi LF, Dalgleish H, et al. Suite2p:
1771 beyond 10,000 neurons with standard two-photon microscopy. bioRxiv. 2017:061507. doi:
1772 10.1101/061507.

1773 107.   Rubinov M, Sporns O. Complex network measures of brain connectivity: Uses and
1774 interpretations. NeuroImage. 2010;52(3):1059-69. PubMed PMID: WOS:000280181800027.

1775 108.   Mizuseki K, Sirota A, Pastalkova E, Buzsaki G. Theta oscillations provide temporal
1776 windows for local circuit computation in the entorhinal-hippocampal loop. Neuron.
1777 2009;64(2):267-80. Epub 2009/10/31. doi: 10.1016/j.neuron.2009.08.037. PubMed PMID:
1778 19874793; PubMed Central PMCID: PMCPMC2771122.

1779 109.   Pedregosa F, Varoquaux G, Gramfort A, Michel V, Thirion B, Grisel O, et al. Scikit-
1780 learn: Machine Learning in Python. J Mach Learn Res. 2011;12:2825-30. PubMed PMID:
1781 WOS:000298103200003.

110. Mathis A, Mamidanna P, Cury KM, Abe T, Murthy VN, Mathis MW, et al. DeepLabCut: markerless pose estimation of user-defined body parts with deep learning. Nat Neurosci. 2018;21(9):1281-9. Epub 2018/08/22. doi: 10.1038/s41593-018-0209-y. PubMed PMID: 30127430.

111. Aarts E, Verhage M, Veenvliet JV, Dolan CV, van der Sluis S. A solution to dependency: using multilevel analysis to accommodate nested data. Nat Neurosci. 2014;17(4):491-6. Epub 2014/03/29. doi: 10.1038/nn.3648. PubMed PMID: 24671065.

112. Bates D, Machler M, Bolker BM, Walker SC. Fitting Linear Mixed-Effects Models Using lme4. J Stat Softw. 2015;67(1):1-48. PubMed PMID: WOS:000365981400001.

113. Kuznetsova A, Brockhoff PB, Christensen RHB. lmerTest Package: Tests in Linear Mixed Effects Models. J Stat Softw. 2017;82(13):1-26. PubMed PMID: WOS:000417711600001.